Redshift-weighted constraints on primordial non-Gaussianity from the clustering of the eBOSS DR14 quasars in Fourier space

Emanuele Castorina,[a,c] **Nick Hand,**[b] **Uroš Seljak,**[a,b,c] **Florian Beutler,**[d] **Chia-Hsun Chuang,**[e,f] **Cheng Zhao,**[g] **Héctor Gil-Marín,**[h] **Will J. Percival,**[i,j] **Ashley J. Ross,**[k] **Peter Doohyun Choi,**[l] **Kyle Dawson,**[m] **Axel de la Macorra,**[n] **Graziano Rossi,**[l] **Rossana Ruggeri,**[d] **Donald Schneider,**[o] **Gong-Bo Zhao**[p]

[a]Berkeley Center for Cosmological Physics, Department of Physics, University of California, Berkeley CA 94720

[b]Department of Astronomy, University of California, Berkeley, CA 94720

[c]Lawrence Berkeley National Laboratory, 1 Cyclotron Road, Berkeley, CA 93720

[d]Institute of Cosmology & Gravitation, University of Portsmouth, Dennis Sciama Building, Portsmouth, PO1 3FX, UK

[e]Leibniz-Institut fur Astrophysik Potsdam (AIP), An der Sternwarte 16, D-14482 Potsdam, Germany

[f]Kavli Institute for Particle Astrophysics and Cosmology, Stanford University, 452 Lomita Mall, Stanford, CA 94305, USA

[g]Laboratoire d'Astrophysique, cole Polytechnique Fdrale de Lausanne, 1015 Lausanne, Switzerland

[h]ICC, University of Barcelona, IEEC-UB, Martí i Franquès, 1, E08028 Barcelona, Spain

[i]Department of Physics and Astronomy, University of Waterloo, 200 University Ave. W., Waterloo ON N2L 3G1, Canada

[j]Perimeter Institute for Theoretical Physics, Waterloo, Ontario N2L 2Y5, Canada

[k]Department of Astronomy, The Ohio State University, 140 W. 18th Ave., Columbus, OH 43210, USA

[l]Department of Physics and Astronomy, Sejong University, 209, Neungdong-ro, Gwangjin-gu, Seoul, South Korea

[m]Department of Physics and Astronomy, University of Utah, 115 S. 1400 E., Salt Lake City, UT 84112, USA

[n]Instituto de Fsica, Universidad Nacional Autnoma de Mxico, Apdo. Postal 20-364, Mxico

[o]Institute for Gravitation and the Cosmos, Pennsylvania State University, University Park, PA 16802, USA

[p]National Astronomical Observatories of China, Chinese Academy of Sciences, 20A Datun Road, Chaoyang District, Beijing 100012, China

Abstract. We present constraints on local primordial non-Gaussianity (PNG), parametrized through $f_{\rm NL}^{\rm loc}$, using the Sloan Digital Sky Survey IV extended Baryon Oscillation Spectroscopic Survey Data Release 14 quasar sample. We measure and analyze the anisotropic clustering of the quasars in Fourier space, testing for the scale-dependent bias introduced by primordial non-Gaussianity on large scales. We derive and employ a power spectrum estimator using optimal weights that account for the redshift evolution of the PNG signal. We find constraints of $-51 < f_{\rm NL}^{\rm loc} < 21$ at 95% confidence level. These are amont the tightest constraints from Large Scale Structure (LSS) data. Our redshift weighting improves the error bar by 15% in comparison to the unweighted case. If quasars have lower response to PNG, the constraint degrades to $-81 < f_{\rm NL}^{\rm loc} < 26$, with a 40% improvement over the standard approach. We forecast that the full eBOSS dataset could reach $\sigma_{f_{\rm NL}^{\rm loc}} \simeq$ 5-8 using optimal methods and full range of scales.

Contents

1   Introduction

Measurements of the statistical properties of the late-time large-scale structure (LSS) of the Universe can provide insights into the physics that generated the primordial density fluctuations. In particular, they offer the possibility to distinguish between different models of cosmic inflation by measuring primordial non-Gaussianity (PNG), the deviation from Gaussian random field initial conditions. In this work, we focus on the local type of PNG, through the one parameter $f_{\rm NL}^{\rm loc}$. Single-field inflationary models predict an amplitude of $f_{\rm NL}^{\rm loc}$ that is unmeasurably small, and a detection of $|f_{\rm NL}^{\rm loc}| \gtrsim 1$ would robustly rule out this class of inflationary models [1, 2].

    The current state-of-the-art constraint on PNG comes not from LSS data but from measurements of the bispectrum of the cosmic microwave background (CMB) by the *Planck* satellite, which has reported $f_{\rm NL}^{\rm loc} = 0.8 \pm 5.0$ [3]. Unfortunately, the improvement in precision from CMB measurements is not expected to reach the level required to distinguish between inflationary models ($\sigma(f_{\rm NL}^{\rm loc}) \sim 1$) due to cosmic variance limitations [4, 5]. However, forecasts for future LSS surveys, e.g., [6–15], indicate a strong potential for PNG constraints. The sensitivity to PNG originates from the distinctive scale-dependent bias signature that is imprinted on the clustering of biased tracers (e.g., galaxies or quasars) by local primordial non-Gaussianity [16–19] (see e.g. [20] for a review). The effect is proportional to the bias of the tracers themselves and scales as $f_{\rm NL}^{\rm loc} k^{-2}$; thus, it is most prominent on the largest

scales probed by a survey. Further gains can be made by surveys that observe multiple tracers, which are able to effectively remove uncertainties from sample variance in their measurements [21–24].

The current best constraints from the analysis of large-scale structure data are comparable to those found by the *WMAP* CMB experiment [18, 25–29]. The first such analysis by [18] combined a number of different tracers from early SDSS releases to find $f_{\rm NL}^{\rm loc} = 28^{+23}_{-24}$ (68% CL). This analysis also demonstrated the constraining power of quasars, finding $f_{\rm NL}^{\rm loc} = 8^{+26}_{-37}$ at 68% CL using only the SDSS photometric quasar sample. For recent constraints using QSOs see [26, 27, 30]. As quasars are highly biased and probe large volumes, they are ideal for measuring the PNG signal on large scales. On the other hand large scales are the most contaminated by systematic effects [25, 28, 31–35]. Systematics control has spurred work on the use of cross-correlations in LSS PNG analyses, e.g., [36, 37].

Data sets that probe large volumes offer the best chance to detect non-Gaussian biasing features on large scales, but they also complicate data analysis. For samples that span a wide redshift range, traditional analysis methods, such as using multiple, smaller redshift bins, become non-optimal. A proper treatment of the redshift evolution of the tracer bias and PNG signal is therefore necessary to fully exploit the constraining power of a data set. Recent work has focused on using redshift weights to optimize LSS surveys for baryon acoustic oscillation (BAO) and redshift-space distortion (RSD) analyses [38–40]. The methods presented in the aforementioned works have been recently applied to the first data release and cosmological analyses of the extended Baryon Oscillation Spectroscopic Survey (eBOSS; [41]) survey [42–46]. The idea of redshift weighting scheme was also extended in [47] to optimize for PNG constraints. The purpose of this work is to present and clarify the methodology to perform an optimal, in a statistical sense, signal weighted measurement of PNG using galaxy surveys data.

Our first goal is to derive a redshift-weighted optimal quadratic estimator for the two-point statistics that yields optimal constraints for $f_{\rm NL}^{\rm loc}$. Our method is general and can be applied to any other parameter, using measurements in configuration space or Fourier space in a spectroscopic or photometric catalog. We will also show that optimal redshift weights to a good approximation change the effective redshift of a survey, in a way that is completely analogous to the standard FKP weights [48]. As an application of our method we use the Sloan Digital Sky Survey (SDSS) IV eBOSS Data Release 14 quasar sample (DR14Q) [49] to derive constraints on $f_{\rm NL}^{\rm loc}$. This data set includes 148,659 quasars and spans a redshift range of $0.8 \leq z \leq 2.2$.

This paper is organized as follows. We present our new optimal estimator, which correctly accounts for redshift evolution of the signal, in §2. In §3 we describe the eBOSS quasar sample used in this work. §4 outlines our analysis methods, including how we estimate the power spectrum multipoles of the data and the theoretical model used to estimate parameters. In §5 we study the Fisher matrix of eBOSS data to try to quantify a-priori the improvement yielded by the optimal analysis. We present our constraints on $f_{\rm NL}^{\rm loc}$ in §6 and discuss and conclude in §7.

2 Primordial Non-Gaussianities in the Large Scale Structure

2.1 Local PNG

In this work we focus on the local type of primordial non-Gaussianity, where the primordial potential, $\Phi_p(\mathbf{x})$, is the sum of a random Gaussian field, ϕ, and its square,

$$\Phi_p(\mathbf{x}) = \phi(\mathbf{x}) + f_{\rm NL}^{\rm loc} \left(\phi(\mathbf{x})^2 - \left\langle \phi^2 \right\rangle \right), \tag{2.1}$$

with $f_{\rm NL}^{\rm loc}$ parametrizing the amount of PNG. The relation between Φ_p and the matter overdensity δ_m is easiest to express in Fourier space, where it is given by $\delta_m(k,z) = \alpha(k,z)\Phi_p(k)$, with

$$\alpha(k,z) = \frac{2c^2 k^2 T(k) D(z)}{3\Omega_m H_0^2} \tag{2.2}$$

where $T(k)$ is the transfer function, c is the speed of light, $D(z)$ is the linear growth factor normalized to $(1+z)^{-1}$ in the matter-dominated era, Ω_m is the matter density parameter at $z = 0$, and H_0 is

the present-day Hubble parameter. We also define a related quantity $\widetilde{\alpha}$, which will be useful in the discussion to follow:

$$\widetilde{\alpha}(k, z) \equiv \frac{2\delta_c}{\alpha(k, z)} = \frac{3\Omega_m H_0^2 \delta_c}{c^2 k^2 T(k) D(z)}, \tag{2.3}$$

with $\delta_c = 1.686$, the critical density in the spherical collapse model in a Einstein-deSitter Universe.

As shown in [16, 18, 19], local PNG as parametrized by $f_{\rm NL}^{\rm loc}$ introduces a scale-dependent bias, $\Delta b(k, z)$, given by

$$\Delta b(k, z) \equiv b_\phi f_{\rm NL}^{\rm loc} \widetilde{\alpha}(k, z) = (b - p) f_{\rm NL}^{\rm loc} \widetilde{\alpha}(k, z), \tag{2.4}$$

where b_ϕ is the response of the halo or galaxy field to the presence of PNG. In the last equality we assumed $b_\phi = (b - p)$ where b is the bias of the sample. This is an approximation to the exact $f_{\rm NL}^{\rm loc}$ response of discrete tracers, but measurements in N-body simulations have shown it is good enough to estimate the amplitude of scale-dependent bias [50]. The parameter p takes a value of 1 for a halo mass selected sample and 1.6 for samples dominated by recent mergers [18, 51], as could be the case for QSOs for instance. For the purpose of deriving an optimal estimator we will not fix p for now. At the linear order, and after adding redshift-space distortions (e.g., [52]), we find the quasar overdensity is related to the matter overdensity in the presence of PNG as follows

$$\delta_{\rm qso} = [b + f\mu^2 + \Delta b]\delta_m \equiv [\widetilde{b} + \Delta b]\delta_m \tag{2.5}$$

where $f = d\ln D/d\ln a$ is the logarithmic growth rate, μ is the cosine of the angle between the Fourier modes and the line of sight, and we have defined the convenient quantity $\widetilde{b} = b + f\mu^2$, which accounts for both Gaussian biasing and linear redshift-space distortions.

2.2 Optimal estimators in LSS

Our goal is to derive an estimator for the two-point clustering of a data set that yields the tightest constraint on $f_{\rm NL}^{\rm loc}$. We begin by describing the data, positions on the sky and redshifts of set of objects, in terms of the pixelized overdensity $\delta_{\rm qso}(\boldsymbol{r}_i)$, where $\boldsymbol{r}_i$ gives the pixel position. We will also need the mean density at a given pixel position, denoted as $\bar{n}(\boldsymbol{r}_i)$. Optimal analysis invariably requires inverse noise weighting of the data. For example, if $\bar{n}(\boldsymbol{r}_i) = 0$ then no data have been observed at that pixel and it should not be used for data analysis, suggesting that the noise should be infinite. An additional source of uncertainty is sample variance, which is caused by the finite number of measureable modes and is present even in absence of noise.

When considering Gaussian statistics, the optimal inverse noise weighting of a data set has a well-defined solution, known as the optimal quadratic estimator [53, 54], which weights the data inversely by the covariance matrix. If we collect our overdensity pixels into a vector $\boldsymbol{x}$, with $x_i = \delta_{\rm qso}(\boldsymbol{r}_i)$, then its signal covariance matrix is S_{ij}, and the total covariance matrix reads

$$C_{ij} = \langle x_i x_j \rangle = N_{ij} + S_{ij} == [V\bar{n}(\boldsymbol{r}_i)]^{-1}\delta_{ij}^K + S_{ij}, \tag{2.6}$$

where δ_{ij}^K is the Kronecker delta, V is the pixel volume, and we have assumed Poisson statistics for the noise term N_{ij}.

The optimal quadratic estimator (OQE) for a parameter θ is then [55–58]

$$\hat{q}_\theta = \frac{1}{2}\boldsymbol{x}^t C^{-1} C_{,\theta} C^{-1} \boldsymbol{x} - \Delta q_\theta, \tag{2.7}$$

where $C_{,\theta}$ denotes the derivative of C with respect to θ, and Δq_θ subtracts a possible bias of the estimator. If the response of the covariance matrix is constant in θ, then the OQE is also the maximum likelihood solution.

The most difficult task is to compute $C^{-1}\boldsymbol{x}$, and a diagonal form for the configuration space covariance matrix C is often employed to evaluate C^{-1}. Suppose indeed we want to determine, using Eq. (2.7), the power spectrum around some k, where we expect the power to be close to a fiducial

power spectrum $P_{\rm fid}$. If we assume that the power spectrum is locally flat (white noise) within the band powers then its Fourier transfer would be a zero lag correlation function determined by the amplitude of the power spectrum. This gives rise to a diagonal inverse of the covariance matrix in configuration space,

$$C_{ij}^{-1} = (P_{\rm fid}(k) + \bar{n}^{-1})^{-1} V \delta_{ij}^K \, . \tag{2.8}$$

The fiducial power spectrum should in principle be varied with k, but over the range of scales one is usually interested in it is a relatively slowly varying function. For PNG, we are concerned with the power on the largest scales, and we can assume a constant fiducial value $P_{\rm fid} \sim 3 \times 10^4 \ h^{-3} {\rm Mpc}^3$ for all wavenumbers k.

We also need to evaluate the derivative $C_{,\theta}$, where θ is the parameter we wish to determine, in our case the averaged value of the power spectrum. Suppose we focus first on a single mode k with a volume $d\boldsymbol{k} = (2\pi)^3/V$. The Fourier transform of the power spectrum is the correlation function, which for this single mode gives $S_{ij} = V^{-1} P(k) \exp[i\boldsymbol{k}(\boldsymbol{r}_i - \boldsymbol{r}_j)]$. Its derivative with respect to $P(\boldsymbol{k})$ gives

$$\frac{dC_{ij}}{dP(k)} = V^{-1} e^{i\boldsymbol{k}(\boldsymbol{r}_i - \boldsymbol{r}_j)}, \tag{2.9}$$

and the estimator of Eq. (2.7) for the power spectrum becomes

$$\hat{P}(k) = A \left| \sum_j e^{i\boldsymbol{k}\boldsymbol{r}_j} w_{\rm FKP} \right|^2 , \tag{2.10}$$

where we have replaced the sum over pixels with the sum over discrete objects, such that $\delta_{\rm qso} \bar{n} V = N_{\rm qso}$, where $N_{\rm qso}$ is the number of objects in the pixel (if the pixels are small enough this can be viewed just as the sum over object positions $\boldsymbol{r}_i$). The weights $w_{\rm FKP}$ take the well-known form as first derived in [48], $w_{\rm FKP} = (1 + \bar{n} P_{\rm fid})^{-1}$. We see that the operation in Eq. (2.10) is a Fourier transform, which can be computed rapidly using fast Fourier transforms (FFTs). The normalization A can be determined by performing the same operation on an unclustered catalog of synthetic objects, including FKP weights, and normalized to the total number of observed objects [48, 59–62].

2.3 Optimal estimator for $f_{\rm NL}^{\rm loc}$

Now we consider instead the weighting scheme that yields an optimal constraint on $f_{\rm NL}^{\rm loc}$. We explicitly account for redshift evolution by considering overdensity pixels as a function of time, or redshift, $\boldsymbol{r} = \boldsymbol{r}(z)$. We begin by computing the signal covariance in the presence of PNG from Eq. (2.5),

$$S_{12} = \langle \delta_{\rm qso}(\boldsymbol{r}_1(z_1)) \delta_{\rm qso}(\boldsymbol{r}_2(z_2)) \rangle \tag{2.11}$$

$$= \left\langle \left[(\widetilde{b}_1 + \Delta b_1) \delta_m(\boldsymbol{r}_1) \right] \left[(\widetilde{b}_2 + \Delta b_2) \delta_m(\boldsymbol{r}_2) \right] \right\rangle, \tag{2.12}$$

where we have defined $\widetilde{b}_1 = \widetilde{b}(z_1)$, $\boldsymbol{r}_1 = \boldsymbol{r}(z_1)$, $\Delta b_1 = \Delta b(z_1)$, and similar quantities at z_2. Evaluating the derivative of this expression at $f_{\rm NL}^{\rm loc} = 0$ yields

$$\left. \frac{dS_{12}}{df_{\rm NL}^{\rm loc}} \right|_{f_{\rm NL}^{\rm loc}=0} = \widetilde{b}_1 (b_2 - p) \widetilde{\alpha}_2 \langle \delta_m(\boldsymbol{r}_1) \delta_m(\boldsymbol{r}_2) \rangle + 1 \leftrightarrow 2 \, , \tag{2.13}$$

where the second term is symmetric and can be computed via an exchange of indices. We can use the definition of the the power spectrum to express this equation as

$$\left. \frac{dS_{12}}{df_{\rm NL}^{\rm loc}} \right|_{f_{\rm NL}^{\rm loc}=0} = (b_1 - p) b_2 \int \frac{d\boldsymbol{k}}{2\pi^3} \widetilde{\alpha}_1(k) (1 + \beta_2 \mu_{r_2}^2) P_m(k, z_1, z_2) e^{i\boldsymbol{k}(\boldsymbol{r}_1 - \boldsymbol{r}_2)} + 1 \leftrightarrow 2, \tag{2.14}$$

where $P_m(k)$ the matter power spectrum, $\beta = f/b$ is the standard RSD parameter, and μ_{r_2} is the line-of-sight angle associated with position $\boldsymbol{r}_2$.

It is useful to factor out some of the time dependencies in equation Eq. (2.14) using

$$P_m(k, z_1, z_2) = P_m(k, z_0)(k)D(z_1)D(z_2)/D(z_0)^2, \tag{2.15}$$

$$\widetilde{\alpha}(k, z) = \frac{\widetilde{\alpha}_0(k)}{D(z)} \,, \tag{2.16}$$

with z_0 some reference time, we adopted $z = 0$. [1] With these definitions, we can express the optimal estimator in Eq. (2.7) as a function of $\boldsymbol{r}_1$ and $\boldsymbol{r}_2$ as

$$
\begin{aligned}
\hat{q}_{f_{\mathrm{NL}}^{\mathrm{loc}}}(\boldsymbol{r}_1, \boldsymbol{r}_2) &= \frac{1}{2}C^{-1}\boldsymbol{x}^t \frac{dS_{12}}{df_{\mathrm{NL}}^{\mathrm{loc}}}\bigg|_{f_{\mathrm{NL}}^{\mathrm{loc}}=0} C^{-1}\boldsymbol{x} - \Delta q_{f_{\mathrm{NL}}^{\mathrm{loc}}} \\
&= \frac{1}{2}\frac{\delta_{\mathrm{qso}}(\boldsymbol{r}_1)}{C}\left[\int \frac{d\boldsymbol{k}}{2\pi^3}e^{i\boldsymbol{k}(\boldsymbol{r}_1-\boldsymbol{r}_2)}P_{m,0}(k)\widetilde{\alpha}_0(k)D(z_2)(1 + \beta_2\mu_{\boldsymbol{r}_2}^2)(b_1 - p)b_2\right. \\
&\quad \left. + \ 1 \leftrightarrow 2\right]\frac{\delta_{\mathrm{qso}}(\boldsymbol{r}_2)}{C} - \Delta q_{f_{\mathrm{NL}}^{\mathrm{loc}}}.
\end{aligned}
\tag{2.17}
$$

And now, summing over $\boldsymbol{r}_1$ and $\boldsymbol{r}_2$, we obtain the estimator

$$
\begin{aligned}
\hat{q}_{f_{\mathrm{NL}}^{\mathrm{loc}}} &= \frac{1}{2}\int \frac{d\boldsymbol{k}}{(2\pi)^3}P_{m,0}(k)\widetilde{\alpha}_0(k) \\
&\quad \left\{\left[\int d\boldsymbol{r}_1 \, e^{i\boldsymbol{k}\boldsymbol{r}_1}\frac{\delta_{\mathrm{qso}}(\boldsymbol{r}_1)}{C}(b_1 - p)\right]\left[\int d\boldsymbol{r}_2 \, e^{-i\boldsymbol{k}\boldsymbol{r}_2}\frac{\delta_{\mathrm{qso}}(\boldsymbol{r}_2)}{C}b_2 D(z_2)(1 + \beta_2\mu_{\boldsymbol{r}_2}^2))\right] \right. \\
&\quad \left. + \ 1 \leftrightarrow 2\right\} - \Delta q_{f_{\mathrm{NL}}^{\mathrm{loc}}}.
\end{aligned}
\tag{2.18}
$$

Note that in these equations the inverse noise weight factors of C^{-1} are identical to those discussed in Section 2.2, with the FKP weight being the near-optimal scheme. We can further decompose in Legendre polynomials the angular part of the Kaiser factor,

$$(1 + \beta\mu^2) = \left(1 + \frac{\beta}{3}\right)\mathcal{L}_0(\mu) + \frac{2}{3}\beta\mathcal{L}_2(\mu) \tag{2.19}$$

then define, for a generic weight $w(z)$, the weighted density multipoles

$$\delta_\ell^w(\mathbf{k}) = \int \mathrm{d}^3r \, e^{i\mathbf{k}\cdot\mathbf{r}} w_{\mathrm{FKP}}(z)w(z)\delta(\mathbf{r})\mathcal{L}_\ell(\hat{k}\cdot\hat{r}) \tag{2.20}$$

to finally obtain

$$\hat{q}_{f_{\mathrm{NL}}^{\mathrm{loc}}} = \int \frac{\mathrm{d}k\, k^2}{2\pi^2}P_{m,0}(k)\widetilde{\alpha}_0(k)\int \frac{d\Omega_k}{4\pi}[\delta_0^{\tilde{w}}(-\mathbf{k})\sum_{\ell=0,2}\delta_\ell^{w_\ell}(\mathbf{k})] - \Delta q_{f_{\mathrm{NL}}^{\mathrm{loc}}} \tag{2.21}$$

where

$$\tilde{w}(z) = b(z) - p \quad , \quad w_0(z) = D(z)(b(z) + f(z)/3) \quad , \quad w_2(z) = 2/3D(z)f(z) \,. \tag{2.22}$$

---

[1]Multiplicative constants independent of wavenumber k and redshift, like $D(z_0)$, can be safely neglected as the final result is always properly normalized.
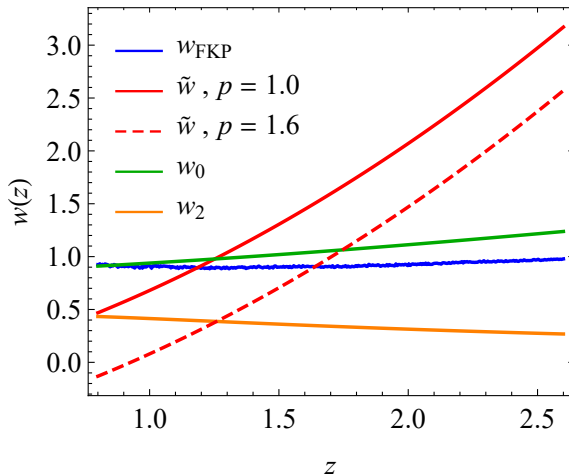
Figure 1: Redshift weights for the eBOSS DR14 QSO catalog. Since $n(z)P_0 \ll 1$, the standard FKP weights, in blue, show small redshift evolution. The optimal weights to estimate PNG are shown in red, green and orange. The weights depend on the QSOs response to $f_{\mathrm{NL}}^{\mathrm{loc}}$, as one can see from the difference between the solid red line, for $p = 1$, and the dashed one, for $p = 1.6$.

The above Eq. (2.21) and the associated set of weights defines the optimal signal weighting of the power spectrum, and they represent one of the main results of this work. One can immediately recognize that, if we neglect the optimal weights, the structure of angular integral over the wavenumber $\boldsymbol{k}$ is the same of standard estimators of the monopole and quadrupole of the power spectrum [59–63]. This is expected, as the optimal redshift weights are no different than FKP weights in this respect. Within our model, the hexadecapole, $\ell = 4$, does not carry any information about PNG and therefore does not appear in the optimal estimator. We notice that optimal weights for PNG up-weight high redshift galaxies, which are highly biased and have therefore larger $f_{\mathrm{NL}}^{\mathrm{loc}}$ response. The OQE also exploits the fact that the primordial potential does not evolve in redshift, whereas the Gaussian part of the signal does. This can be seen by comparing the different dependence of $\tilde{w}$ and w_ℓ on the linear growth function $D(z)$. Figure 1 shows the redshift evolution of the unormalized weights in the eBOSS DR14 QSOs catalog, described in more details in Section 3. For the DR14 sample, $w_{\mathrm{FKP}}(z)$, blue line, and $w_\ell(z)$, green and orange lines, slowly vary across the survey, the former since $n(z)P_0 \ll 1$ whereas the latter because $b_{\mathrm{qso}}(z)D(z) \simeq \mathrm{const}$. One the other hand $\tilde{w}(z)$ grows quite rapidly with resdhift, up-weighting galaxies with a larger response to $f_{\mathrm{NL}}^{\mathrm{loc}}$.

Finally, the estimator in Eq. (2.21) in principle needs to be made unbiased by subtracting out the signal in the absence of any $f_{\mathrm{NL}}^{\mathrm{loc}}$ via the $\Delta q_{f_{\mathrm{NL}}^{\mathrm{loc}}}$ term. As we will see in the next section, optimal weighting boils down to a redefinition of the mean redshift of the survey, allowing us to use standard tools to constrain $f_{\mathrm{NL}}^{\mathrm{loc}}$ or other parameters, and obtain statistically unbiased results. It is also straightforward to generalize the estimator defined above to the case of cross-correlation between different tracers.

We conclude this section with a few remarks. Our estimator differs from the one in [47], in which the authors defined optimal weights for pairs of galaxies, under the assumption that a single redshift can be associated to each pair. The drawback of this approach is that there is no straightforward implementation in Fourier Space, as there is no Fourier space analog of a pair of objects. This led [47] to define weights for individual galaxies as a square root of pair weights. However, weights can be negative and one is forced to take an absolute value before the square root. We'd like to stress that configuration and Fourier space carry the same amount of information, and as such the same weighting scheme should apply to both. Our method naturally addresses this issue, as the optimal weights are defined for each individual object. The same arguments hold for the weights derived in [40] for redshift-space distortions parameters and for BAO in [39].

3 Data

In this section, we describe the eBOSS DR14Q sample and the synthetic mock catalogs used in our analysis.

3.1 eBOSS DR14Q sample

The extended Baryon Oscillation Spectroscopic Survey [41] is part of the SDSS-IV experiment [64]. The eBOSS cosmology program relies on the same optical spectrographs [65] as the SDSS-III BOSS survey, installed on the 2.5 meter Sloan Foundation Telescope [66] at the Apache Point Observatory in New Mexico. In addition to observing luminous red galaxies and emission line galaxies, eBOSS will observe and measure redshifts for $\sim$500,000 quasars across a volume of the Universe unexamined by previous spectroscopic surveys. First eBOSS cosmology results for the DR14Q sample were recently presented in [67], which reported the first BAO distance measurement in the range $1 < z < 2$. The clustering properties of the eBOSS quasars have also been previously examined in [68, 69], although these works do not make use of the full DR14Q sample. Recent work in [42–46, 70, 71] has presented several application of eBOSS DR14 data to measurements of BAO and redshift space distortions parameters.

The imaging data, target selection, and catalog construction methods for the DR14Q sample used in this work are discussed in detail in [49, 72]. Targets are selected from the catalogs of the SDSS I/II surveys [73], released as part of SDSS DR7 [74], and the SDSS-III survey [75, 76], released as part of SDSS DR8 [77]. The eBOSS also makes use of several bands of the Wide Field Infrared Survey Explorer (WISE; [78]), as described in [79]. The target selection criteria for the DR14Q sample is presented in detail in [80, 81].

Accurate redshift estimation is crucial for achieving the cosmology goals of eBOSS, which is particularly challenging for quasar spectra [82]. As described in [72], the DR14Q sample contains three automated redshift estimates per object. In this work, we use the so-called "fiducial" redshift $z_{\rm fid}$, which can be any of the three redshift estimates, depending on which one yields the lowest catastrophic failure rate (see [72] for further details).

The DR14Q sample contains 148,659 objects with spectroscopic redshifts in the range $0.8 \leq z \leq 2.2$. The observed objects are distributed in two separate angular regions in the North Galactic Cap (NGC) and South Galactic Cap (SGC). The effective areas of these regions are 1214.6 deg^2 and 899.3 deg^2, respectively. We show the observed number density as a function of redshift for the NGC and SGC regions in Figure 2. There are slight discrepancies in $n(z)$ between the two regions due to differences in targeting efficiency.

3.2 Completeness weights

Objects in the DR14Q sample are assigned weights to account for the incompleteness of the target selection process and other systematic effects that could potentially bias our clustering measurements. There are two main types of weights that we will discuss in this section, spectroscopic completion weights $w_{\rm spec}$ and systematic imaging-based weights $w_{\rm sys}$. The former accounts for the fact that a small percentage of targets do not receive a redshift while the latter set of weights corrects for systematics arising from photometric inhomogeneities in the targeting selection. When combining these two sets of weights, we take the total completeness weight as

$$w_{\rm c} = w_{\rm sys} \cdot w_{\rm spec}. \tag{3.1}$$

3.2.1 Spectroscopic weights

The first main cause of spectroscopic incompleteness in the DR14Q sample is *fiber collisions*. Fiber collisions result when a pair of quasars are separated by less than the $62''$ angular size of the SDSS spectrograph fiber, which prevents one of the objects from being observed. Missed observations are partially alleviated by the eBOSS tiling pattern, which naturally has overlapping tiles in regions with a density of targets on the sky, and thus, allows redshifts to be measured for objects separated by
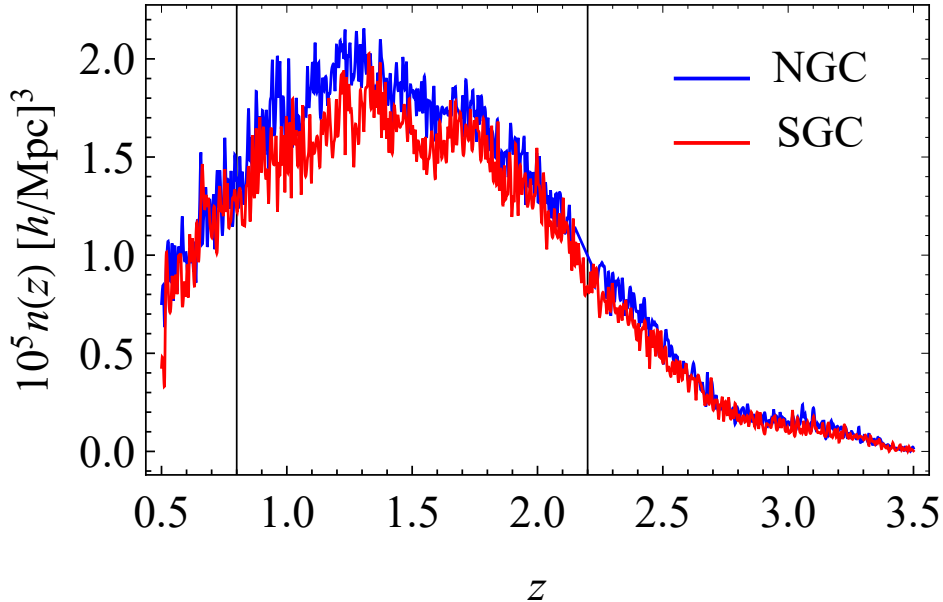
Figure 2: The mean density of quasars in the DR14Q sample as a function of redshift for the NGC (blue) and SGC (red) regions of the sky. The differences between the two regions are due to known discrepancies with the targeting efficiency. The two vertical lines bracket the DR14 QSOs in $0.8 < z < 2.2$.

less than the $62''$ collision scale. Ultimately, 4% and 3% of the eBOSS quasar targets are fiber-collided objects that do not receive a spectroscopic observation in the NGC and SGC regions, respectively.

We account for the missing objects due to fiber collisions by up-weighting the nearest neighbor with a valid redshift and spectroscopic class. This procedure follows previous clustering analyses, e.g., as in BOSS [83, 84]. In practice, this is not a perfect correction, as a fraction of fiber collision pairs are mere projections and are not associated with the same dark matter halo. However, the nearest neighbor weighting scheme does preserve the large-scale bias of the clustering sample. As we are concerned only with the PNG signal on large scales, we leave exploration of most advanced fiber collision correction schemes, e.g., [85], for future work. We denote the weight used to correct for fiber collisions as a *close pair* weight, w_{cp}. By default, its value is unity for all objects that are not involved in a fiber collision, and for the case of fiber collisions, it is equal to an integer with value greater than unity.

The second main cause of spectroscopic incompleteness is *redshift failures*, which refers to the subset of quasars that do not receive a valid automated redshift and are not visually inspected. The distribution of these objects is not uniform within the focal plane due to variations in detector efficiency. In past BOSS releases [86], redshift failures were an almost negligible fraction of the total, less than 1%. However, redshift determination for a quasar at $z \sim 1.5$ is more difficult than for an LRG at $z \sim 0.5$, and the DR14Q sample has a redshift failure rate of 3.4% and 3.6% in the NGC and SGC, respectively. With this increased rate, a more complex scheme than was used in previous BOSS analyses, is required to adequately correct for the effect. Here, we use a focal plane weight w_{foc} defined as

$$w_{foc} = [1 - P_{rf}(x_{foc}, y_{foc})]^{-1}, \tag{3.2}$$

where P_{rf} defines the probability of obtaining a redshift failure as a function of position in the focal plane. With this weight, quasars with measured redshifts that are observed in positions on the focal plane where P_{rf} is greater than zero will be up-weighted to account for the fact that, on average,

targeted quasars are missing from the sample due to redshift failures. We refer the reader to [71] for further details on the redshift failure weights.

Finally, we assign the total spectroscopic completeness weight as the product of the fiber collision and redshift failure weights, $w_{\mathrm{spec}} = w_{\mathrm{cp}} \cdot w_{\mathrm{foc}}$.

3.2.2 Imaging weights

Each quasar in the DR14Q sample is also assigned a weight to mitigate photometric systematics, using the prescription studied in [68]. The weights, denoted here as w_{sys}, account for inhomogeneities in the quasar targeting selection related to the Galactic extinction and depth of the targeting image data. The weights used in this work have been utilized in previous eBOSS cosmology analyses [67, 71]. They are described in detail in section 3.4 of [67], and we refer the reader to that work for further details.

3.3 Synthetic DR14Q catalogs

We make use of a set of mock catalogs to estimate the covariance matrix of the eBOSS power spectrum measurements. The mocks are based on the Extended Zel'dovich (EZ) approximate N-body simulation scheme [87]. Throughout this work, we refer to this set of synthetic catalogs as EZ mocks. In total, we utilize 1000 independent realizations for each Galactic cap region. We also use the mocks to verify and test our analysis and parameter estimation pipelines.

The set of EZ mocks are generated following the methodology outlined in [87], matching both the angular footprint and redshift selection function of the DR14Q sample. Briefly, the EZ mock scheme relies on the Zel'dovich approximation to generate a density field, and implements nonlinear and halo biasing effects through the use of free parameters. These free parameters are tuned to produce two-point and three-point clustering of a desired data set. The method allows for the fast generation of a large number of mock catalogs without the computational cost of full N-body simulations, and it has been used extensively in previous BOSS cosmology analyses, e.g., [88, 89].

The EZ mock catalogs account for the redshift evolution of the eBOSS quasars by constructing a light-cone out of 7 redshift shells, generated from periodic boxes of side length $L = 5000\ h^{-1}\mathrm{Mpc}$ at different redshifts. The free parameters of each box are calibrated independently, and the boxes are combined using the make_survey software [90]. The background density field of the light cone mocks is continuous, as each of the boxes shares the same initial Gaussian density field. The NGC and SGC data sets are treated independently when deriving the best-fit internal EZ mock parameters. The cosmology of the EZ mocks is a flat, ΛCDM model with $\Omega_m = 0.307115$, $\Omega_b = 0.048206$, $h = 0.6777$, $\sigma_8 = 0.8255$, and $n_s = 0.9611$.

Finally, we mirror the effects of fiber collisions and redshift failures (as discussed in section 3.2.1) and each object in an EZ mock catalog also has associated values for w_{foc} and w_{cp}. Fiber collisions are implemented by applying the tiling pattern to the mock data, and removing pairs that fall within the collision scale that are not in overlapping tiles. Redshift failures are applied by statistically removing objects based on the position of the object in the focal plane, using the probability of a redshift failure $P_{\mathrm{rf}}(x_{\mathrm{foc}}, y_{\mathrm{foc}})$.

4 Analysis Methods

Throughout our analysis, we assume a flat ΛCDM cosmology from [91] as our fiducial background cosmology. The parameter set we use is $h = 0.6774$, $\Omega_b h^2 = 0.0223$, $\Omega_c h^2 = 0.1188$, $n_s = 0.9667$, and $\sigma_8 = 0.8159$. We use this fiducial cosmology to convert observed quasar coordinates (right ascension, declination, and redshift) to Cartesian coordinates during the estimation of the power spectrum of the sample (see §4.1). The fiducial cosmology also determines the shape of the real-space matter power spectrum, which is used in our theoretical modeling (see §4.2).

4.1 Power spectrum estimation

We begin by defining the weighted quasar density fields [48]

$$\tilde{F}(\boldsymbol{r}) = \tilde{w}_{\mathrm{tot}} \left[n'_{\mathrm{qso}}(\boldsymbol{r}) - \alpha'_{\mathrm{s}} n_{\mathrm{s}}(\boldsymbol{r}) \right] \quad , \quad F_\ell(\boldsymbol{r}) = w_{\mathrm{tot},\ell} \left[n'_{\mathrm{qso}}(\boldsymbol{r}) - \alpha'_{\mathrm{s}} n_{\mathrm{s}}(\boldsymbol{r}) \right] , \qquad (4.1)$$

where n'_{qso} and n_{s} are the number densities of the quasar sample and a synthetic catalog of random objects, respectively. The total weights are the product of FKP and the optimal redshift weights

$$\tilde{w}_{\mathrm{tot}}(z) = w_{\mathrm{FKP}}(z)\tilde{w}(z) \quad , \quad w_{\mathrm{tot},\ell}(z) = w_{\mathrm{FKP}}(z)w_\ell(z) \;, \tag{4.2}$$

and they are applied to both the quasar and synthetic samples. The synthetic catalog contains unclustered objects – it is used to define the expected mean density of the survey, accounting for the radial and angular selection functions. The factor α'_{s} gives the ratio of quasars to synthetic objects and serves to properly normalize the number density of the synthetic catalog. In our notation, quantities marked with a prime ($\prime$) include the completeness weights w_{c} specified in Section 3.2. The synthetic catalog defines our expected number density, and as such, does not require completeness weights. The synthetic sample has a number density $1/\alpha'_{\mathrm{s}}$ times more dense than the true sample. We assume that, on average, the relation $\langle n'_{\mathrm{qso}}(\boldsymbol{r})\rangle = \alpha'_{\mathrm{s}}\langle n_s(\boldsymbol{r})\rangle$ holds true. We define α'_{s} as $\alpha'_{\mathrm{s}} = N'_{\mathrm{qso}}/N_{\mathrm{s}}$, where $N'_{\mathrm{qso}} = \sum_{\mathrm{qso}} w_c$ and N_{s} is the total number of objects in the synthetic catalog.

Now, the multipoles of the cross-correlation between the weighted density fields can be estimated following [59],

$$\hat{P}_\ell = \frac{2\ell+1}{A_\ell} \int \frac{d\Omega_k}{4\pi} \left[\int d\boldsymbol{r}_1 \; \tilde{F}(\boldsymbol{r}_1) e^{i\boldsymbol{k}\cdot\boldsymbol{r}_1} \int d\boldsymbol{r}_2 \; F_\ell(\boldsymbol{r}_2) e^{-i\boldsymbol{k}\cdot\boldsymbol{r}_2} \mathcal{L}_\ell(\hat{\boldsymbol{k}}\cdot\hat{\boldsymbol{r}}_2) \right] - S_\ell, \tag{4.3}$$

where we have introduced the shot noise contribution S_ℓ, defined as

$$S_\ell = A_\ell^{-1} \int d\boldsymbol{r} \; n'_{\mathrm{qso}}(\boldsymbol{r})(w_{\mathrm{c}}(\boldsymbol{r}) + \alpha'_{\mathrm{s}})\tilde{w}_{\mathrm{tot}}w_{\mathrm{tot},\ell}(\boldsymbol{r})\mathcal{L}_\ell(\hat{\boldsymbol{k}}\cdot\hat{\boldsymbol{r}}), \tag{4.4}$$

which is different than zero only for the monopole $\ell = 0$. The normalization is defined as

$$A_\ell = \int d\boldsymbol{r} \; w_{\mathrm{tot},\ell}(\boldsymbol{r})\tilde{w}_{\mathrm{tot}}(\boldsymbol{r})[n'_{\mathrm{qso}}(\boldsymbol{r})]^2 \;. \tag{4.5}$$

We compute the shot noise (equation 4.4) and the normalization (equation 4.5) as discrete sums over the quasar and synthetic catalogs. To do so, we make use of the following relation:

$$\int d\boldsymbol{r} \; n'_{\mathrm{qso}}(\boldsymbol{r}) \ldots \longrightarrow \sum_i^{N_{\mathrm{qso}}} w_{\mathrm{c}}(\boldsymbol{r}_i) \ldots \longrightarrow \alpha'_{\mathrm{s}} \sum_i^{N_{\mathrm{s}}} \ldots, \tag{4.6}$$

where the integral can be expressed equivalently as a sum over the quasar or synthetic catalogs. Thus, the normalization A_ℓ can be computed as

$$A_\ell = \sum_i^{N_{\mathrm{qso}}} n'_{\mathrm{qso}}(\boldsymbol{r}_i)w_c(\boldsymbol{r}_i)w_{\mathrm{tot},\ell}(\boldsymbol{r}_i)\tilde{w}_{\mathrm{tot}}(\boldsymbol{r}_i) \tag{4.7}$$

$$= \alpha'_{\mathrm{s}} \sum_i^{N_{\mathrm{s}}} n_s(\boldsymbol{r}_i)w_{\mathrm{tot},\ell}(\boldsymbol{r}_i)\tilde{w}_{\mathrm{tot}}(\boldsymbol{r}_i) \;. \tag{4.8}$$

Note that while equations 4.7 and 4.8 are equivalent on average, in practice, we use the latter equation to estimate the normalization due to the increased number density of the synthetic catalog. Similarly, we can express the shot noise contribution to the monopole (equation 4.4) as

$$S_0 = A_0^{-1} \left[\sum_i^{N_{\mathrm{qso}}} w_{\mathrm{c}}^2(\boldsymbol{r}_i)\tilde{w}_{\mathrm{tot}}(\boldsymbol{r}_i)w_{\mathrm{tot},0}(\boldsymbol{r}_i) + \alpha'^2_{\mathrm{s}} \sum_i^{N_{\mathrm{s}}} \tilde{w}_{\mathrm{tot}}w_{\mathrm{tot},0}(\boldsymbol{r}_i) \right], \tag{4.9}$$

where the two terms compute the contributions to the shot noise from the quasar and synthetic catalogs, respectively. There is some uncertainty surrounding the impact of fiber collisions and completeness weights on the Poisson shot noise calculation of equation 4.9 [92–94]. We choose to use the

standard Poisson expression and vary a shot noise parameter while performing parameter estimation to account for any discrepancies (see section 4.2).

Our implementation of equation 4.3 uses the FFT-based estimator of [62]. This estimator builds upon similar estimators presented in [60, 61], but reduces the number of FFTs required per multipole using a spherical harmonic decomposition. We calculate the power spectrum multipoles as

$$\hat{P}_\ell(k) = \frac{2\ell+1}{A_\ell} \int \frac{d\Omega_k}{4\pi} \tilde{F}(\boldsymbol{k}) F_\ell(-\boldsymbol{k}), \tag{4.10}$$

with

$$
\begin{aligned}
F_\ell(\boldsymbol{k}) &\equiv \int d\boldsymbol{r}\; F_\ell(\boldsymbol{r}) e^{i\boldsymbol{k}\cdot\boldsymbol{r}} \mathcal{L}_\ell(\hat{\boldsymbol{k}}\cdot\hat{\boldsymbol{r}}), \\
&= \frac{4\pi}{2\ell+1} \sum_{m=-\ell}^{\ell} Y_{\ell m}(\hat{\boldsymbol{k}}) \int d\boldsymbol{r}\; F_\ell(\boldsymbol{r}) Y_{\ell m}^*(\hat{\boldsymbol{r}}) e^{i\boldsymbol{k}\cdot\boldsymbol{r}},
\end{aligned}
\tag{4.11}
$$

where $Y_{\ell m}$ are spherical harmonics. Note that equation 4.11 requires the calculation of $2\ell+1$ FFTs for a multipole of order ℓ.

To compute the FFTs required by our estimator, we estimate the overdensity field on a mesh of 1024^3 cells for the quasar and synthetic catalogs using a Triangular Shaped Cloud (TSC) interpolation scheme (see e.g., [95]). When interpolating to the mesh, each quasar contributes a weight of $w_c w_{\text{tot}}$ and each synthetic object a weight of w_{tot}. When computing FKP weights, we use a fiducial power spectrum value of $P_0 = 3 \times 10^4\; h^{-3}\text{Mpc}^3$, roughly equal to the expected power on the scales where PNG is prominent in our sample, $k \simeq 0.03\; h\text{Mpc}^{-1}$. We use the interlaced grid technique of [95, 96] to limit the effects of aliasing, and we correct for any artifacts of the TSC scheme using the correction factor of [97]. With the combination of TSC interpolation and interlacing, we are able to measure the power spectrum multipoles up to $k = 0.4\; h\text{Mpc}^{-1}$ with fractional errors at the level of 10^{-3} [96]. To perform these operations, as well as estimate the power spectrum multipoles via equation 4.10, we utilize the massively parallel implementations available as part of the open-source Python toolkit nbodykit [98].

4.2 Modeling

4.2.1 The power spectrum model

We use linear theory to predict the quasar power spectrum in redshift-space [52]

$$P_{\text{qso}}(k,\mu) = G(k,\mu;\sigma_P)^2 \left[b_{\text{tot}}(k) + f\mu^2\right]^2 P_m(k) + N, \tag{4.12}$$

where P_m is the real-space matter power spectrum, N is a free parameter accounting for residual shot noise, and b_{tot} is the total quasar bias, including PNG, given by

$$b_{\text{tot}}(k) = b_{\text{qso}} + \Delta b = b_{\text{qso}} + f_{\text{NL}}^{\text{loc}}(b_{\text{qso}} - p)\tilde{\alpha}(k), \tag{4.13}$$

where b_{qso} is the linear bias of the quasar sample, and $\tilde{\alpha}$ is defined in Eq. (2.3). To account for redshift-space related damping of the power spectrum, we include a Lorentzian damping function,

$$G(k,\mu;\sigma_P) = \left[1 + (k\mu\sigma_P)^2/2\right]^{-1}, \tag{4.14}$$

with a single free parameter σ_P, which represents the typical damping velocity dispersion. The physical motivation for the inclusion of $G(k,\mu)$ is the Finger-of-God (FOG) effect in redshift space due to the virial motions of the quasar within its host dark matter halo [99]. However, the damping term also accounts for errors in the spectroscopic redshift determination of the quasars [41]. The effect can be estimated for the DR14Q sample as $\sigma_z = 300$ km s^{-1} for $z < 1.5$ and $\sigma_z = [400 \cdot (z - 1.5) + 300]$ km s^{-1} for $z > 1.5$ [41].

The multipoles of the power spectrum are then computed as

$$P_{\ell,\mathrm{qso}}(k) = \frac{2\ell+1}{2} \int_{-1}^{1} d\mu P_{\mathrm{qso}}(k,\mu)\mathcal{L}_\ell(\mu), \tag{4.15}$$

We evaluate the linear, real-space matter power spectrum $P_m(k)$ and the transfer function in Δb using the `classylss` software [100], which provides Python bindings of the `CLASS` CMB Boltzmann solver [101]. We evaluate the linear power spectrum using the fiducial cosmology and keep the shape of the power spectrum fixed during parameter estimation. This choice assumes that the uncertainty as determined by [3] for most of the parameters which define the shape of the power spectrum is much smaller than the uncertainty of our measurement and can be neglected. This has been shown to be a reasonable assumption for current data sets, e.g., [92, 102].

4.2.2 Window function and effective redshift

The measured power spectrum multipoles are the result of the convolution of the true underlying power spectrum with the Fourier transform a window function $W(\mathbf{s})$, defined by the footprint on the sky and the redshift selection function. It is easy to see that the ensemble average of the estimator in Eq. (4.3) measures the following multipoles of the power spectrum $P_{A,eff}(k)$ [63, 103–105]

$$P_{A,eff}(k) = (2A+1) \int \frac{d\Omega_k}{4\pi} \, \mathrm{d}^3 s_1 \, \mathrm{d}^3 s_2 \, e^{i\mathbf{k}(\mathbf{s}_2-\mathbf{s}_1)} \delta(\mathbf{s}_1)\delta(\mathbf{s}_2)W(\mathbf{s}_1)W(\mathbf{s}_2)\mathcal{L}_A(\hat{k}\cdot\hat{s}_1) \tag{4.16}$$

$$= (-i)^A (2A+1) \sum_{\ell,\, L} \begin{pmatrix} \ell & L & A \\ 0 & 0 & 0 \end{pmatrix}^2 \int \mathrm{d}s \, s^2 j_A(ks) \int \mathrm{d}s_1 \, s_1^2 \, \xi_\ell(s; s_1(z)) Q_L(s; s_1(z)) \tag{4.17}$$

where we have defined the multipoles of the window function

$$Q_L(s) \equiv (2L+1) \int \mathrm{d}\Omega_s \int \mathrm{d}^3 s_1 W(\mathbf{s}_1)W(\mathbf{s}+\mathbf{s}_1)\mathcal{L}_L(\hat{s}\cdot\hat{s}_1) \tag{4.18}$$

$$\equiv \int \mathrm{d}s_1 \, s_1^2 \, Q_L(s; s_1). \tag{4.19}$$

In the above equations we have chosen the direction to one of the two QSOs to be the line of sight for the multipole decomposition, $s_1(z)$, explicitly accounting for the redshift evolution of the signal. In principle, one should perform the redshift integral $\int \mathrm{d}\, s_1(z)$ in Eq. (4.16) for each evaluation of the model parameters in the likelihood, which makes the data analysis numerically quite challenging. However, as we will now show, an effective redshift approximation is often very close to the full answer in Eq. (4.16).

Under a generic set of weights $w(z)$ of the density field δ, the effective redshift is defined as

$$z_{\mathrm{eff}} = \frac{\int dz \, n(z)^2 [\chi^2/H(z)] \, w(z)^2 z}{\int dz \, n(z)^2 [\chi^2/H(z)] w(z)^2} \tag{4.20}$$

and the power spectrum evaluated at the effective redshift reads

$$P_A(k; z_{\mathrm{eff}}) = (-i)^A (2A+1) \sum_{\ell,\, L} \begin{pmatrix} \ell & L & A \\ 0 & 0 & 0 \end{pmatrix}^2 \int \mathrm{d}s \, s^2 j_A(ks) \xi_\ell(s; z_{\mathrm{eff}}) Q_L(s) \tag{4.21}$$

For FKP weights and smoothly varying selection function the above expression is sub-percent accurate, even in large redshift bins [106]. In particular, on scales where linear theory is a good approximation, it is always possible to define an effective redshift because in linear theory redshift evolution preserves the shape of the power spectrum. For the DR14 QSOs in NGC, neglecting for the moment the angular mask, assuming the fiducial cosmological parameters and the model in Eq. (4.12), the accuracy of the effective redshift approximation is shown in the left hand panel of Figure 3 for FKP weights. For NGC, between $0.8 \leq z \leq 2.2$ the effective redshift is $z_{\mathrm{eff}} = 1.52$. The measured monopole power spectrum, in blue, can be accurately described by a model evaluated at the effective redshift of the

survey, with deviations smaller than 1%. Moreover the difference between Eq. (4.21) and Eq. (4.16) is well captured by a constant, which can therefore absorbed when marginalizing over galaxy bias. Similar conclusions hold for the quadrupole. The large difference at high k is a mere consequence of the fact that the quadropole crosses zero at $k \simeq 0.25 \, h \, \mathrm{Mpc}^{-1}$, the relative deviation is still quite small. The bottom line is that, within FKP weighting, the error introduced by evaluating the model at an effective redshift is always well below the measurement uncertainties.

Our optimal weights are smooth in redshift, thus we expect to be able to evaluate the theoretical model at new effective redshifts, one for the monopole

$$z_{0,\mathrm{eff}} = \frac{\int dz \ n(z)^2 [\chi^2/H(z)] \ w_{FKP}^2 \tilde{w}(z) w_0(z) z}{\int dz \ n(z)^2 [\chi^2/H(z)] w_{FKP}^2 \tilde{w}(z) w_0(z)} \ , \tag{4.22}$$

and one for the quadrupole

$$z_{2,\mathrm{eff}} = \frac{\int dz \ n(z)^2 [\chi^2/H(z)] \ w_{FKP}^2 \tilde{w}(z) w_2(z) z}{\int dz \ n(z)^2 [\chi^2/H(z)] w_{FKP}^2 \tilde{w}(z) w_2(z)} \ . \tag{4.23}$$

Since the optimal analysis up-weights high-redshift galaxies where the PNG signal is larger, the effective redshift goes up compared to the FKP-only case, $z_{\mathrm{eff}} = 1.52$, to

$$z_{0,\mathrm{eff}} = 1.64 \ , \ z_{2,\mathrm{eff}} = 1.58 \ , \tag{4.24}$$

for $p = 1.0$, and to

$$z_{0,\mathrm{eff}} = 1.74 \ , \ z_{2,\mathrm{eff}} = 1.70 \ , \tag{4.25}$$

for $p = 1.6$. For an optimally weighted case the comparison between the effective redshift approximation, Eq. 4.21, and the full integral over redshift, Eq. 4.16, is shown in the right hand panel of Figure 3. We find that despite the large redshift range covered by eBOSS QSOs, evaluating the power spectrum at the effective redshift is accurate at the percent level for both the monopole and the quadropole. We have further tested this assumptions in mock catalogs, finding that we can reproduce the weighted clustering using the effective redshifts defined above.

We finally stress that effective redshifts can be defined using optimal weights with respect to any other cosmological parameter, and thus, upon checking they provide an accurate description of the data, vastly simplify the cosmological analysis. For instance, see [107] for an implementation of the effective redshift approximation for BAO and RSD in eBOSS data.

The shape of the window function multipoles $Q_L(s)$ and their effect on the monopole of the eBOSS QSOs power spectrum at z_{eff} is shown in Figure 4. The main effect of the survey mask is to reduce the amplitude of clustering at large scales compared to the true underlying power spectrum, and therefore needs to be properly taken into account for unbiased estimates of PNG. Given the high effective redshift and the small fraction of the sky covered by DR14Q, wide angle effects in redshift space distortions and their possible coupling to the survey mask can be safely neglected [63, 104].

4.3 Parameter estimation

In summary, our base model has three free parameters in each patch of the sky: the linear bias b_1, the damping velocity dispersion σ_P, and the shot noise parameter N. When fitting for PNG, we introduce $f_{\mathrm{NL}}^{\mathrm{loc}}$ as an additional free parameter. Since we are not interested in BAO information or RSD we keep cosmological parameters fixed to Planck best fit values and do not include the Alcock-Paczynski (AP) effect [108]. Actually, the onset of the PNG signal is fixed by the position of the wavenumber associated with the size of the horizon at matter-radiation equality, which is one of the most precise derived parameters measured by Planck [91, 109]. Since we have shown that the optimal quadratic estimator, in the limit of diagonal pixel covariance, boils down to a standard measurement of the power spectrum, we don't need to remove the any estimator bias and just model the expected signal. We estimate the best-fit parameters of the model using a likelihood analysis. We assume that the probability that our data vector $\boldsymbol{D}$ corresponds to a realization of our model $\boldsymbol{T}(\boldsymbol{\theta})$ is given by a multi-variate Gaussian of the form,
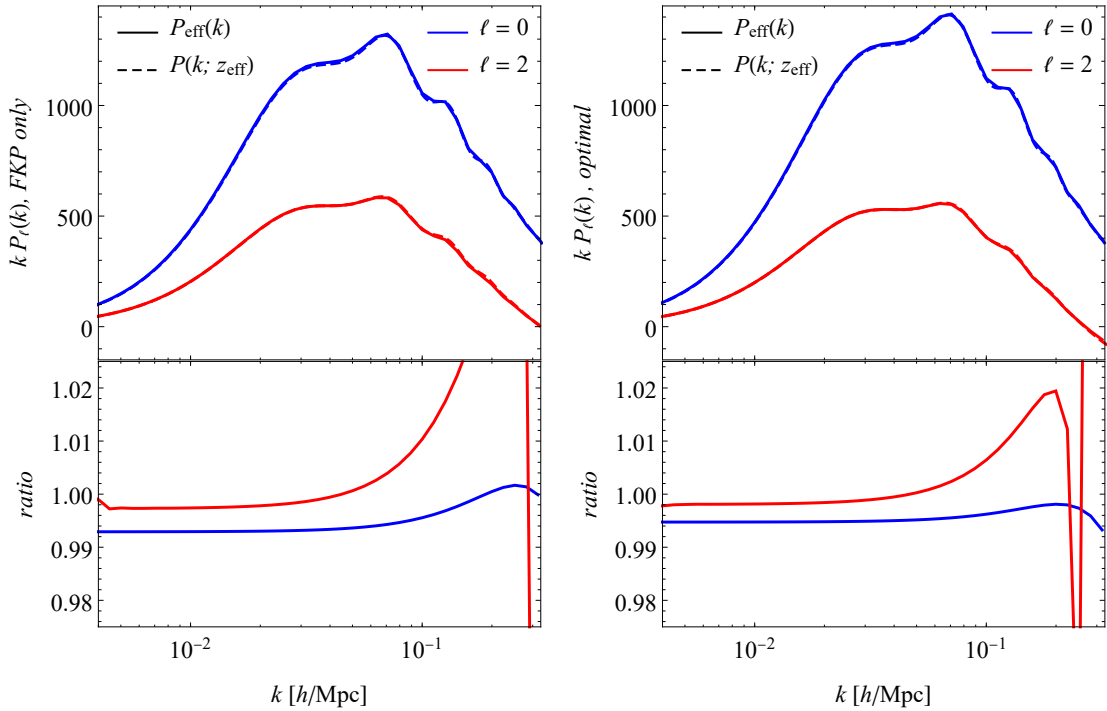
Figure 3: Accuracy of the effective redshift approximation for the eBOSS DR14 QSOs sample (NGC). *Left panel*: The monopole, blue lines, and quadrupole, red lines, evaluated at the effective redshift defined by FKP weights, dashed lines, compared to the full integral of the signal power spectrum over the QSOs selection function, continuous lines. The accuracy for both the monopole and quadrupole is at a percent level, well withing the error in the measurements. *Right panel*: Same as the left panel but including $f_{\mathrm{NL}}^{\mathrm{loc}}$ optimal weights. The amplitude and shape of the multipoles of the power spectrum have changed compared to the plot on the left, but new effective redshift can be defined to provide an excellent description of the full redshift integral.

$$\mathcal{L}(\boldsymbol{D}|\boldsymbol{\theta},\boldsymbol{\Phi}) \propto \exp\left[-\frac{1}{2}\chi^2(\boldsymbol{D},\boldsymbol{\theta},\boldsymbol{\Phi})\right], \tag{4.26}$$

where $\boldsymbol{\theta}$ is our vector of model parameters, and χ^2 takes the quadratic form,

$$\chi^2(\theta) = \sum_{ij}(D_i - T_i(\boldsymbol{\theta}))\Phi_{ij}(D_j - T_j(\boldsymbol{\theta})), \tag{4.27}$$

and $\boldsymbol{\Phi}$ is the inverse of the covariance matrix $\boldsymbol{C}$, often referred as the precision matrix.

When performing our likelihood analysis, our data vector $\boldsymbol{D}$ consists of the monopole and quadrupole, measured using the procedure outlined in section 4.1. We use linearly spaced bins of width $\Delta k = 0.001\ h\mathrm{Mpc}^{-1}$. With the first bin separation at $k \sim 0.005\ h\mathrm{Mpc}^{-1}$ and extending to $k_{\max} = 0.3\ h\mathrm{Mpc}^{-1}$, we have a total of 120 data points in $\boldsymbol{D}$ (60 bins per multipole).

We estimate the covariance matrix of our data measurement using the 1000 EZ mock realizations, described previously in section 3.3. As the covariance is computed from a finite number of mock realizations, its inverse $\boldsymbol{\Phi}$ provides a biased estimate of the true precision matrix due to the skewed nature of the inverse Wishart distribution [110]. To correct for this bias, we re-scale the precision matrix as

$$\boldsymbol{\Phi}' = \frac{N_{\mathrm{mock}} - n_b - 2}{N_{\mathrm{mock}} - 1}\boldsymbol{\Phi}. \tag{4.28}$$
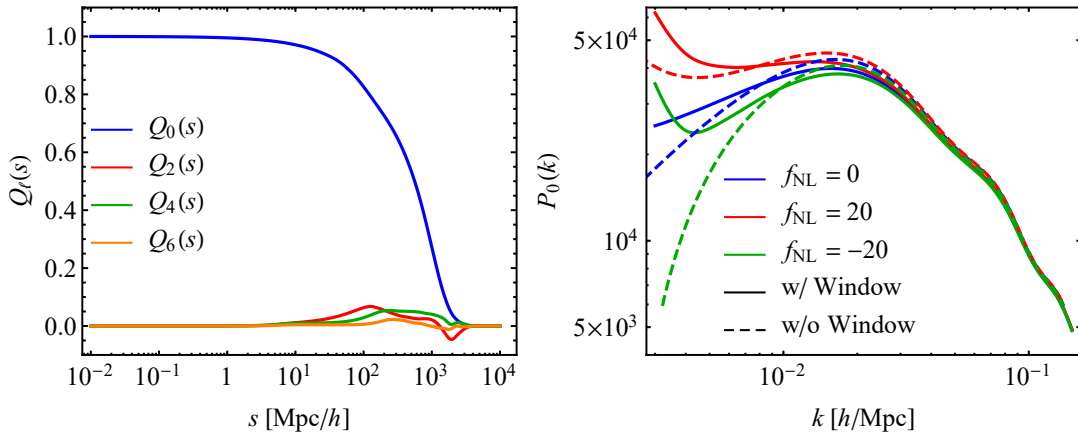
Figure 4: The window function multipoles in configuration space (left) and the effects of the window function on linear Kaiser power spectrum multipoles (right) for the eBOSS DR14Q NGC survey geometry. In the right panel, the solid lines show the original multipoles, while the dashed lines correspond to the model after convolution with the window function, $\hat{P}_\ell(k)$. The main consequence of the presence of the survey geometry is a change in power on large scales.

We performing our likelihood analysis following equation 4.26, we use the rescaled precision matrix $\mathbf{\Phi}'$. In our analysis, we use $N_{\mathrm{mocks}} = 1000$ and $n_b = 120$, yielding a Hartlap factor of ~ 0.88. Following [71] we do not include the extra correction of [111] since it has a minor impact on the errors.

We find the best-fitting model parameters using the LBFGS nonlinear minimization algorithm [112]. We verify that the minimization procedure converges by starting the algorithm from a number of different initialization states. We compute the full posterior distribution of the parameters of interest using the `emcee` software [113] to perform Markov chain Monte Carlo (MCMC) sampling. We assume broad, uniform priors on all parameters of interest such that the priors serve only to bound the parameter values to the largest possible physically meaningful parameter space; they do not have an impact on our derived posterior distributions.

5   Fisher Information

It is useful to look at what a Fisher analysis [114] based on eBOSS number densities and sky area returns for the error on $f_{\mathrm{NL}}^{\mathrm{loc}}$ using measurements of scale-dependent bias. This will tell us the best possible constraints, and on how much improvement we can expect from an optimal analysis.

For simplicity we will assume shot-noise and the redshift error σ_v are perfectly known, as they both have a small impact on the final $f_{\mathrm{NL}}^{\mathrm{loc}}$ bounds. Since we are interested in quantifying the maximum information of the survey we assume QSOs in NGC and SGC have the same value of linear bias. We consider measurements of the monopole and quadrupole only, for which the Fisher matrix reads

$$F_{ij} = V \int_{k_{\min}}^{k_{\max}} \frac{\mathrm{d}k\, k^2}{2\pi^2} \frac{\partial \mathbf{P}(k)}{\partial \theta_i}^{\mathrm{T}} \mathbf{C}(k)^{-1} \frac{\partial \mathbf{P}(k)}{\partial \theta_j} \tag{5.1}$$

where $\theta = \{b_{\mathrm{qso}}, f_{\mathrm{NL}}^{\mathrm{loc}}\}$, $\mathbf{P}(k) = \{P_0(k), P_2(k)\}$ is a vector formed by the monopole and quadrupole of the power spectrum, and $\mathbf{C}(k)^{-1}$ is the inverse of the covariance matrix of the measurements. The fiducial value for the QSO bias is taken from the fitting function in [68], while the fiducial redshift error from [41].

The Fisher matrix can be evaluated at the effective redshift defined by FKP weights or by the optimal ones. In both cases $\sigma_{f_{\mathrm{NL}}^{\mathrm{loc}}}$ is defined via $(\sqrt{F^{-1}})_{22}$. The DR14 catalog contains QSOs from redshift $0.5 < z < 3.5$, of which the redshift range $0.8 < z < 2.2$ corresponds to the fiducial survey. We will repeat the calculation in both redshift ranges, to assess the gains of an extended, in redshift,
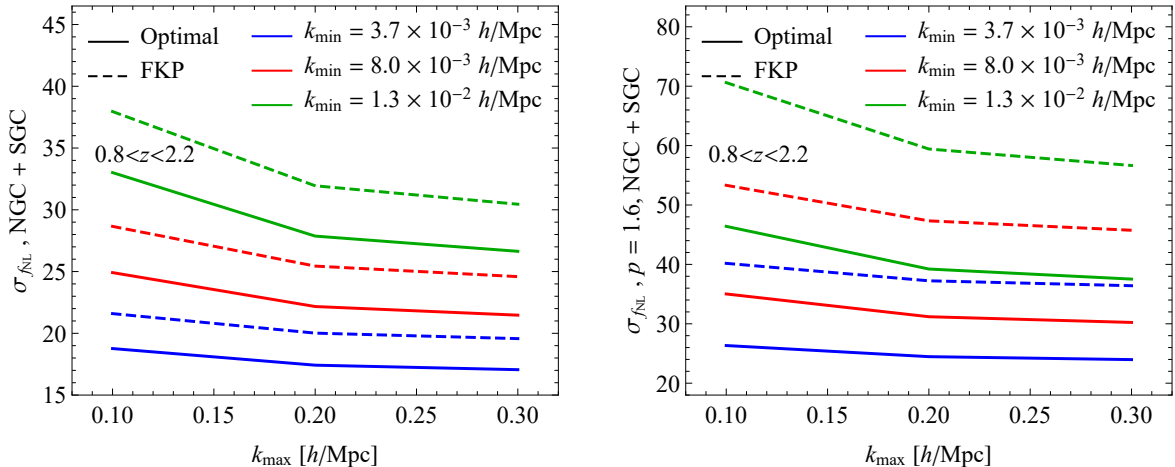
Figure 5: Constraints on PNG from a combined analysis of NGC and SGC in the redshift range $0.8 < z < 2.2$. Different colors corresponds to different value of $k_{\min}$. Dashed lines show the FKP only weights, whereas continuous lines refer to the optimal analysis. Left and right panels correspond to $p = 1.0$ and $p = 1.6$ respectively.

analysis. We furthermore distinguish between NGC and SGC, and thus perform two separate Fisher calculations which are then added together. NGC covers a larger area of the sky than SGC, by $\simeq 30\%$, and will therefore be more constraining. As discussed in Section 2, Eqs. 2.4 and 4.13, the response of a generic tracer to the presence of PNG depends on one parameter p, that for QSOs takes a value between 1 and 1.6. We therefore repeat the Fisher matrix calculation, and in Section 6 the fit to the data, for both values of $p = 1, 1.6$.

5.1 Fiducial Survey: $0.8 < z < 2.2$

The left panel of Figure 5 shows the constraints on $f_{\rm NL}^{\rm loc}$, for $p = 1$, in NGC plus SGC, as a function of $k_{\max}$ and for different values of $k_{\min}$. The values of $k_{\min}$ correspond to the first three k-bins of the measured power spectra. The dashed lines correspond to the FKP weighting, while the continuous one to the optimal analysis. The error $\sigma_{f_{\rm NL}^{\rm loc}}$ strongly depends on the largest scales included in the analysis, since the signal peaks at low k, but it very weakly changes with $k_{\max}$. Comparing the standard analysis to the optimal one, we find that the optimal method provides roughly 20% better error bars than the FKP one, with larger improvement for higher values of $k_{\min}$. The right panel in Figure 5 displays the results of the Fisher analysis for $p = 1.6$. The optimal analysis for $p = 1.6$ moves the effective redshift further up, in order to compensate for the reduced response to $f_{\rm NL}^{\rm loc}$. We thus expect, compared to $p = 1$, larger difference with respect to the FKP-only weighting. We indeed find 40-60% benefit of the optimal analysis comparing it to a standard one. A comparison of the two panels in Figure 5 also shows that $\sigma_{f_{\rm NL}^{\rm loc}}$ degrades by almost a factor of 2 going from $p = 1$ to $p = 1.6$ in the standard FKP analysis, whereas with our method we lose only 50% of the constraining power.

It is worth emphasizing again that we do not know the exact value of p for the eBOSS QSOs sample. This implies that an analysis of the eBOSS data assuming $p = 1$ or $p = 1.6$ will not necessarily return the error bar of the Fisher calculation described above. It is nonetheless reasonable to expect that, in absence of systematic effects at low-k, $\sigma_{f_{\rm NL}^{\rm loc}} \lesssim 20$ and $\sigma_{f_{\rm NL}^{\rm loc}} \lesssim 30$, for $p = 1$ and $p = 1.6$ respectively, are in the reach of eBOSS DR14Q data.

5.2 Including QSOs at $z > 2.2$

The analysis of the previous section suggests that extending the $f_{\rm NL}^{\rm loc}$ analysis to $z > 2.2$ could significantly increase the sensitivity to PNG. The benefit of a larger redshift coverage is two-fold. First, at fixed $k_{\min}$, sample variance is reduced in a larger volume simply because more modes are available. The error $\sigma_{f_{\rm NL}^{\rm loc}}$ indeed roughly scales with $V^{1/2}$ at fixed $k_{\min}$, see Eq. (5.1). Second, since
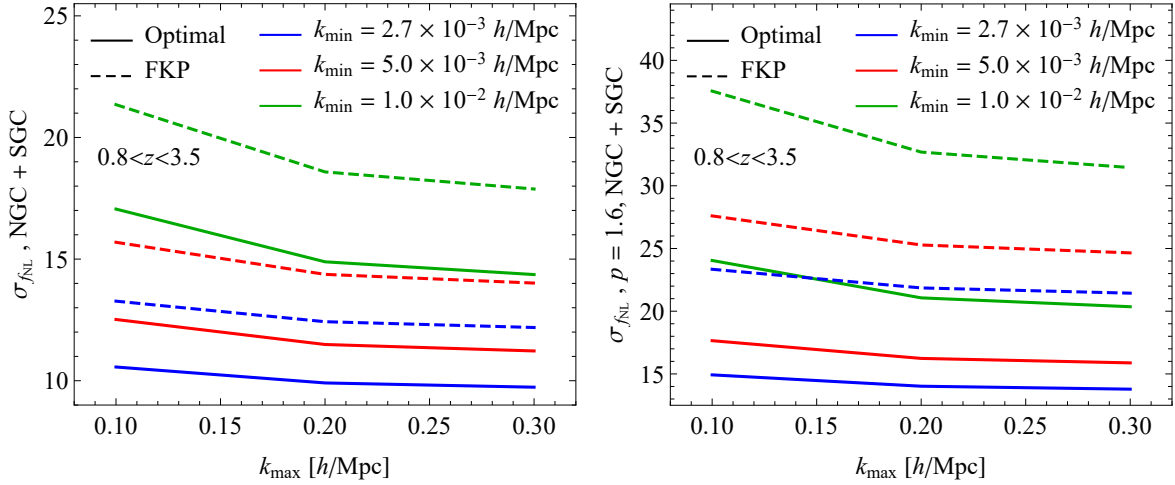
Figure 6: Constraints on f_{NL}^{loc} using DR14Q in $0.8 < z < 3.5$, encompassing the full redshift range of eBOSS. Left and right panel correspond to $p = 1$ and $p = 1.6$ respectively. Note the difference in scale of the y-axis between the two panels.

the signal peaks at the largest scales, including lower k modes into the analysis shrinks the error bars by another factor of $V^{1/6}$. The latter improvement would however require a careful study of the systematic effects at large scale, as described in Section 3.2.1. In this section we calculate the Fisher information of the full redshift range covered by the eBOSS survey, providing a motivation to further investigate and reduce the systematics at low k. The redshift distribution of eBOSS QSOs is such that at $z > 2.5$ the number of objects drops very quickly. In terms of the effective redshift defined in Section 4.2.2 we find

$$0.8 < z < 2.5 \; : \quad z_{eff} = 1.54 \; , \quad \begin{cases} z_{eff,0} = 1.72 \, , \; z_{eff,2} = 1.66 \, , & \text{for } p = 1 \\ z_{eff,0} = 1.83 \, , \; z_{eff,2} = 1.78 \, , & \text{for } p = 1.6 \end{cases} \tag{5.2}$$

and

$$0.8 < z < 3.5 \; : \quad z_{eff} = 1.56 \; , \quad \begin{cases} z_{eff,0} = 1.78 \, , \; z_{eff,2} = 1.69 \, , & \text{for } p = 1 \\ z_{eff,0} = 1.89 \, , \; z_{eff,2} = 1.82 \, , & \text{for } p = 1.6 \, . \end{cases} \tag{5.3}$$

The inclusion of QSOs in the range $2.2 < z < 2.5$ basically does not change the FKP effective redshift, but it moves up the optimal effective redshift by a substantial amount compared to Eq. (4.25). This indicates that a large amount of signal could become accessible by including $z < 2.5$ QSOs in the analysis. Minor shifts in the effective redshift are produced by adding QSO all the way to $z = 3.5$, suggesting that this redshift range will likely only help to reduce sample variance.

Figure 6 shows the error on PNG, $\sigma_{f_{NL}^{loc}}$, that could be obtained by optimally combining all the eBOSS data between $0.8 < z < 3.5$. Several choices of k_{min} are displayed, to help understand how the lack of control on systematics on the largest scales affects the final result. Similarly to what we find in the nominal DR14 redshift range, the optimal analysis yields 25-30% improvement for $p = 1$, and 40-50% for $p = 1.6$. We notice that only in the case of the optimal weighting the full survey could in principle achieve $\sigma_{f_{NL}^{loc}} \simeq 10$, even at relatively high k_{min}. The final eBOSS footprint is expected to be roughly 3 times larger than the one of DR14, which could in principle shrink $\sigma_{f_{NL}^{loc}}$ by an additional $3^{1/2}$. A survey like eBOSS could therefore achieve an error as low as $\sigma_{f_{NL}^{loc}} \simeq 5\text{-}8$, depending on the value of f_{NL}^{loc} response, if systematics can be kept under control.
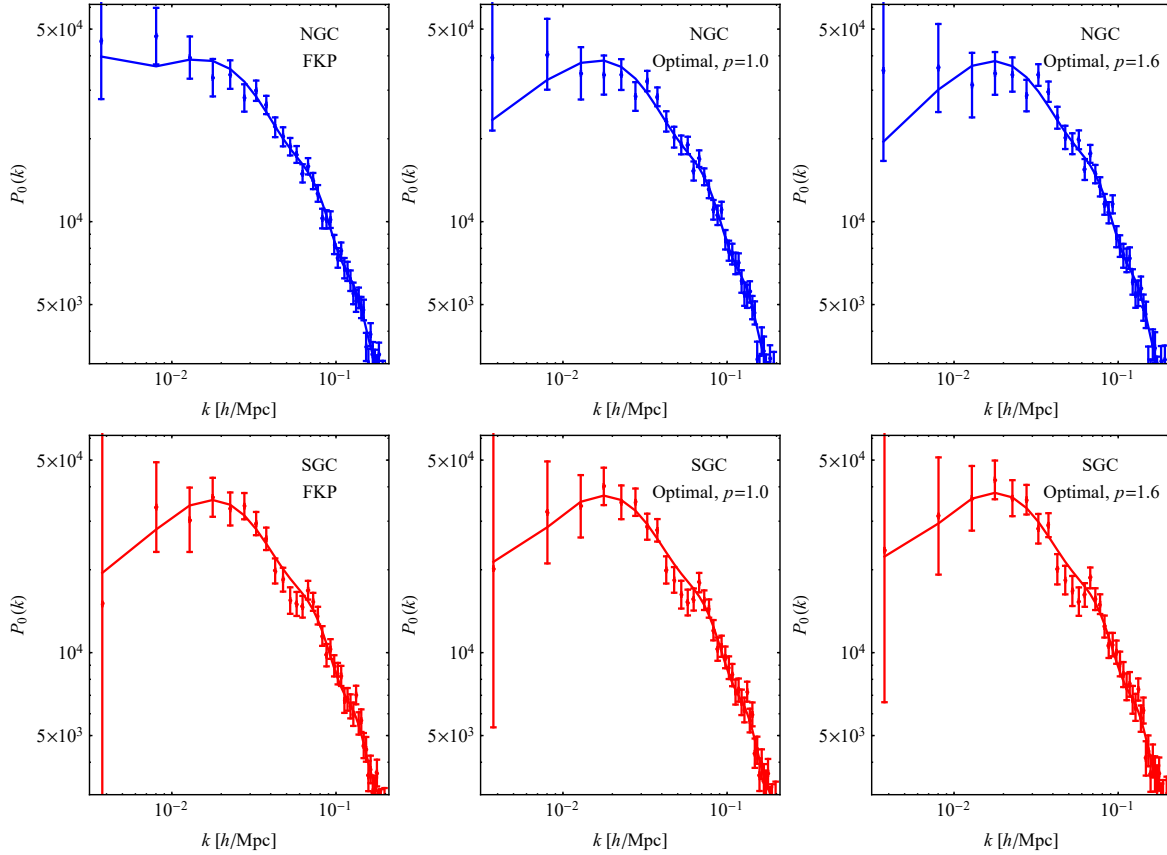
Figure 7: Measurements, points with error bars, and best fit theoretical models, continuous lines, of the monopole power spectrum of the eBOSS DR14 QSOs. The top row shows the power spectra in NGC and the lower ones in SGC.

6 eBOSS DR14 constraints on Primordial Non Gaussianities

We now move to the analysis of the DR14Q catalog. Given the different targeting efficiency in the two patches we treat NGC and SGC separately, with two different values of bias, velocity dispersion and shot noise. This implies that the constraints on $f_{\rm NL}^{\rm loc}$ will not be as tight as in the idealised Fisher calculation.

The first thing we notice in the measured power spectra is that the redshift-space quadrupole in NGC shows an excess of power on large scales not compatible with a cosmological signal. In this paper we therefore focus on the monopole only, which does not show sign of contamination at low-k that could cause a biased estimate of PNG. It is worth keeping in mind that generically residual foregrounds will affect $\ell = 2$ stronger than $\ell = 0$, and that systematic effects can only add power to the monopole of the power spectrum. So as long as there is no detection, an upper limit on $f_{\rm NL}^{\rm loc}$ should be reliable. Since we work at fixed shape of the power spectrum, the quadrupole is almost irrelevant for the final constraint on $f_{\rm NL}^{\rm loc}$, but could become important if the growth factor, or equivalently Ω_m, is allowed to vary. A brief description of the inconsistency of the quadrupole data can be found in Appendinx A.

In Figure 7 we show the measurements, points with error bars, of the monopole of the power spectrum of eBOSS DR14Q in the two regions of the sky, NGC in the upper plots and SGC in the lower ones. The three columns correspond to the standard FKP weighting of the data, and the optimal redshift weighting for $p = 1.0$ and $p = 1.6$. The best fit models, including $f_{\rm NL}^{\rm loc}$ as a free parameter, are displayed as the continuous lines and provide an excellent fit to the data, $\chi_{\rm d.o.f.}^2 \simeq 1$ in all cases.
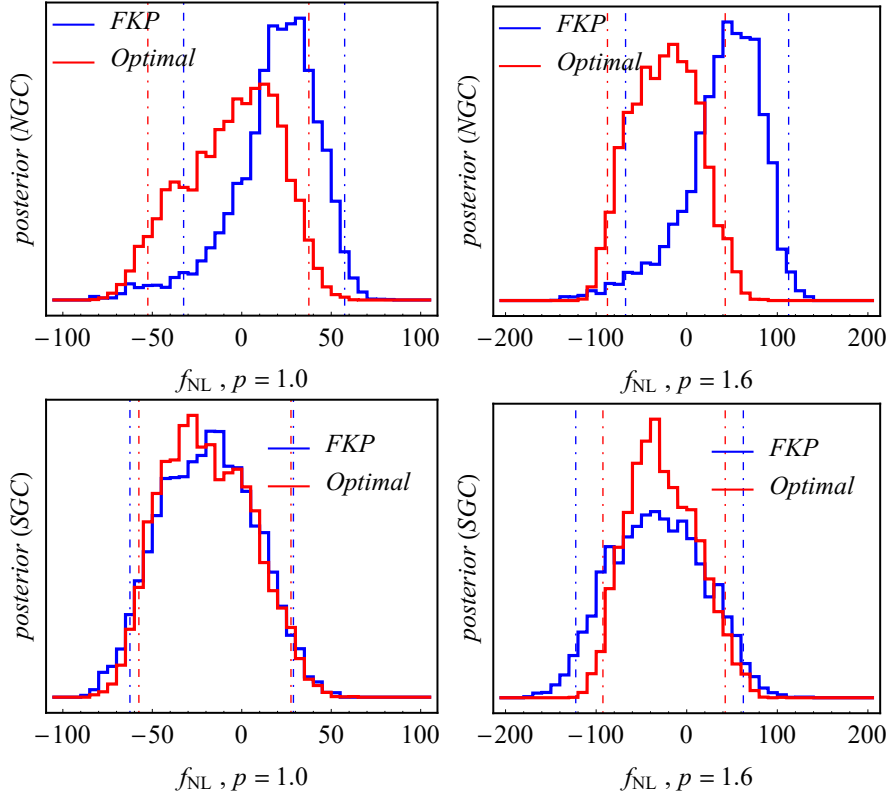
Figure 8: The 1-dimensional posterior of $f_{\mathrm{NL}}^{\mathrm{loc}}$ from separate fits to the NGC (upper panels) and SGC (lower panels). The red histograms show the optimal weighting while the blue ones the FKP weighting. Dot-dashed lines indicate 95% confidence intervals.

Figure 8 shows the one dimensional posterior of $f_{\mathrm{NL}}^{\mathrm{loc}}$ for the different measurements. The first thing worth pointing out is the non-Gaussian posteriors. One expects this because the response to the negative $f_{\mathrm{NL}}^{\mathrm{loc}}$ is very different to the positive $f_{\mathrm{NL}}^{\mathrm{loc}}$, as seen in the right panel of Figure 4. It could be explained by the fact that negative $f_{\mathrm{NL}}^{\mathrm{loc}}$ is a worse fit for FKP weights, and for NGC in particular, see Figure 7, unless $|f_{\mathrm{NL}}^{\mathrm{loc}}|$ is very large and the bias is much larger than the fiducial value of [68]. Non-Gaussian posteriors make the comparison between the FKP and the optimal analysis more difficult, in general there is no unique procedure to compare the two. In all the panels, the dot-dashed lines correspond to the narrowest region encompassing 95% of the area under the posterior, the highest posterior density interval. The actual numbers at 95% confidence level for both patches of the sky can be found in Table 1.

The optimal analysis, in red, always returns smaller 95% c.l. intervals, as it can be most easily noticed in the lower right panel. For $p = 1.0$ we find that in NGC the 95% confidence interval for the optimal analysis is very close to the FKP one (but 10% smaller at 99.7%), and it is 5% smaller in SGC (15% smaller at 99.7%). Compared to the Fisher analysis we therefore find smaller gains for the optimal weighting. For $p = 1.6$, the optimal analysis improves considerably over FKP, with the 95% c.l. now 35-40% smaller for both NGC and SGC. Despite NGC being larger than SGC we do not find any appreciable difference between the two in constraining power on PNG, which could be a statistical fluctuation, or an indication of some systematic differences. Even though it is not significant enough to bias our results, it should be further investigated in new data releases of eBOSS, which will have better statistics.

The best possible constraints on $f_{\mathrm{NL}}^{\mathrm{loc}}$ correspond to the joint analysis of NGC and SGC, for which the results are shown in Figure 9. The left panels show the $f_{\mathrm{NL}}^{\mathrm{loc}}$ posterior, while the right shows QSOs bias parameters for the two areas of the sky. At 68 (95)% confidence level we find
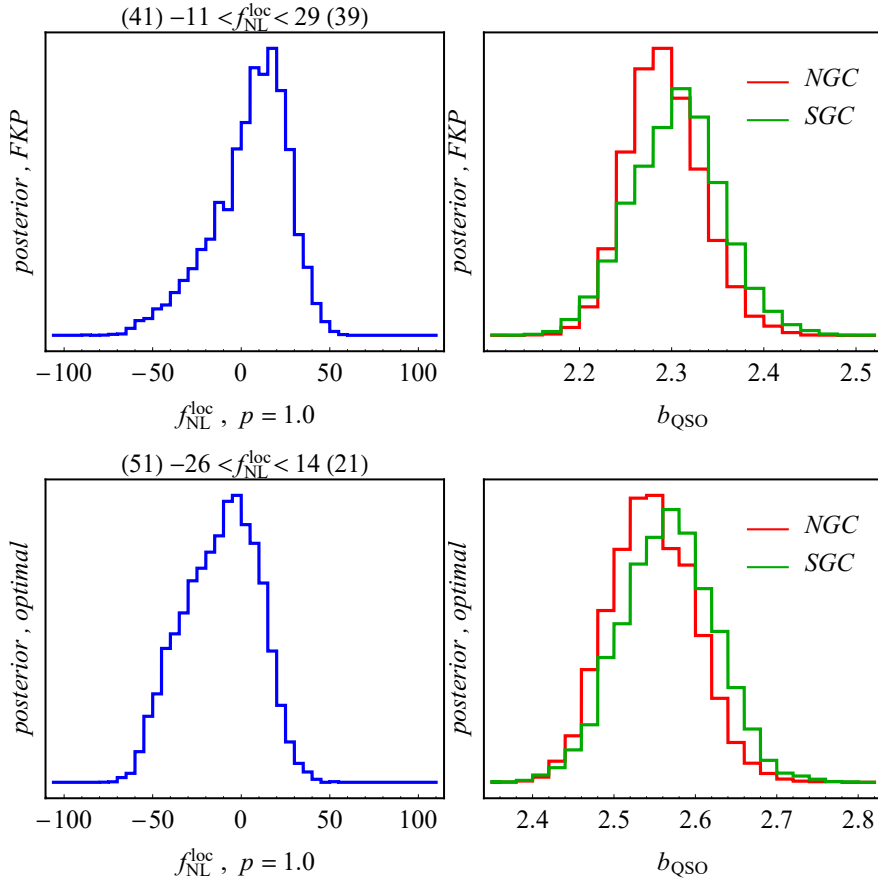
Figure 9: Posterior distribution from jointly fitting the NGC and SGC sky regions, assuming $p = 1.0$ for the f_{NL}^{loc} response. *Left:* 1-dimensional posteriors of f_{NL}^{loc} (blue). *Right:* The 1-dimensional posteriors for the QSO bias in NGC (red) and SGC (green). The upper panels show the FKP weighting, while the lower ones show the optimal weighting.

$(41) - 11 < f_{NL}^{loc} < 29 (39)$ for NGC+SGC, $p = 1.0$ and FKP weights. In the optimal case the constraint reads $(51) - 26 < f_{NL}^{loc} < 14 (21)$. In the combined NGC+SGC case the FKP analysis is therefore 10% worse than the optimal one. As expected the QSO bias has increased in the optimal case, in accordance with the higher effective redshift of the survey. For $p = 1.6$ the joint constraints on PNG are shown in 10. The improvement of the optimal analysis is more than 35%. It is also important to notice that the optimal weights make the difference between the constraints on f_{NL}^{loc} for the two values of p much smaller compared to ones in the FKP case, where $p = 1.6$ is almost a factor of 2 worse than $p = 1.0$. Since the true response of any discrete tracer will never be exactly known, our results shows the importance of optimal signal to noise weighting in making this extra source of uncertainties less important.

The numbers given above are among the tightest constraints on PNG using LSS data, and the most stringent one using spectroscopy data of a single tracer. Given the much smaller area of the sky and number of objects compared to [18, 34], our analysis strongly indicates the 3D information is crucial to achieve tight constraints on PNG. At the same time our work makes clear that much more effort should be devoted to studying systematic effects at large angular separation, and remove those modes altogether if a proper foreground cleaning procedure cannot be found [27, 31, 35, 62].

Optimal weights also help in reducing degeneracies between f_{NL}^{loc} and other parameters. Figure 11 shows the 2-dimensional posterior of f_{NL}^{loc} and the QSOs bias in NGC (similar results hold in SGC). The FKP case is shown in the left panels, and for $p = 1.0$ and $p = 1.6$ in the upper and lower plots,
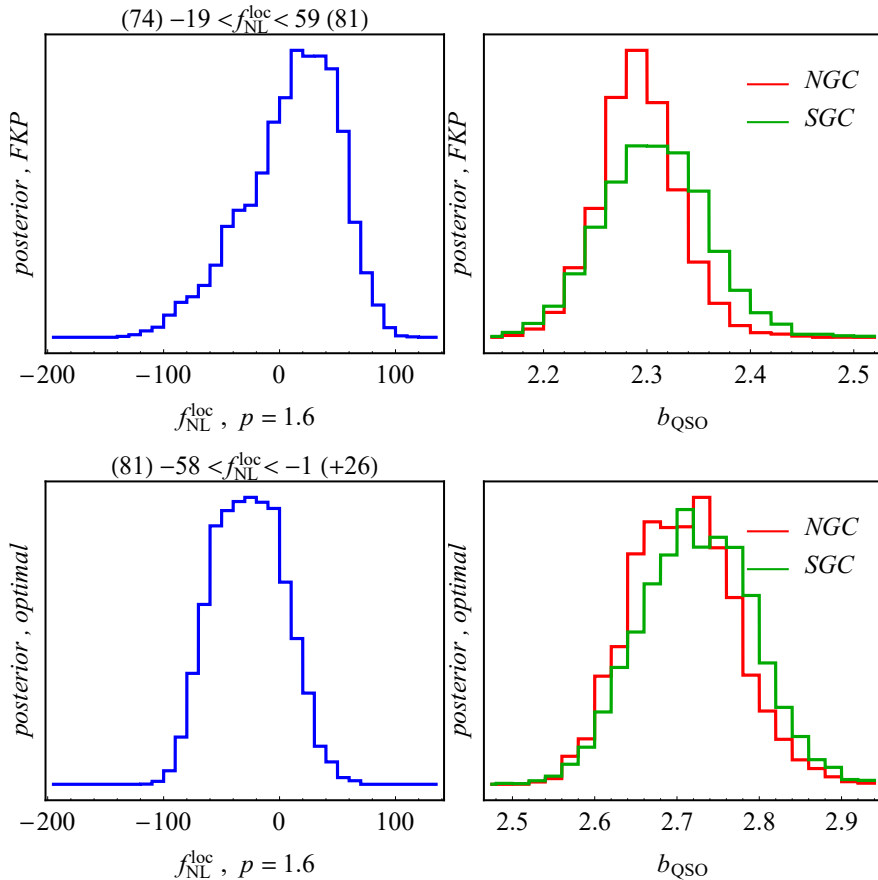
Figure 10: Posterior distribution from jointly fitting the NGC and SGC sky regions, assuming $p = 1.6$ for the $f_{\rm NL}^{\rm loc}$ response. *Left:* 1-dimensional posteriors of $f_{\rm NL}^{\rm loc}$ (blue). *Right:* The 1-dimensional posteriors for the QSO bias in NGC (red) and SGC (green). The upper panels show the FKP weighting, while the lower ones show the optimal weighting.

respectively. Comparison with the optimal analysis on the right hand panels shows that the optimal weights help shrinking the 2-dimensional contours and the correlation between $f_{\rm NL}^{\rm loc}$ and the QSOs bias. A summary of the constraints on $f_{\rm NL}^{\rm loc}$ can be found in Table 1. We repeated the analysis removing the first k-bin, and found an increase of 20-30% in errors as compared to the analysis including all the bins presented above.

Finally, we would like to comment on the use of mocks to validate the constraints we get from the data. The EZ mocks have not been tuned to reproduce the $f_{\rm NL}^{\rm loc}$ response b_ϕ of the eBOSS data, as the latter is unknown. One would need full physics simulations of the specific eBOSS QSOs sample in order to at least have a theoretical prior on the value of p, and consistently compare the constraints on the mocks with the ones obtained in the data. This implies that, if the PNG response of the sample is poorly determined, mocks can only be used to estimate the covariance matrix of the measurements at the fiducial value of $f_{\rm NL}^{\rm loc} = 0$. We also found that the way the mocks have been generated, with BAO and RSD as their primary goals, does not guarantee that the power spectrum on the largest scales correctly reproduce linear theory. We indeed find a small discrepancy, not significant compared to the expected cosmic variance of the measurements, between the mocks and the theory at the largest scales, that to the best of our knowledge cannot be attribute to modeling systematics. We were nevertheless able to check that even in the mocks the optimal analysis improves over the standard FKP one, but the actual mock constraints cannot be compared with the data.
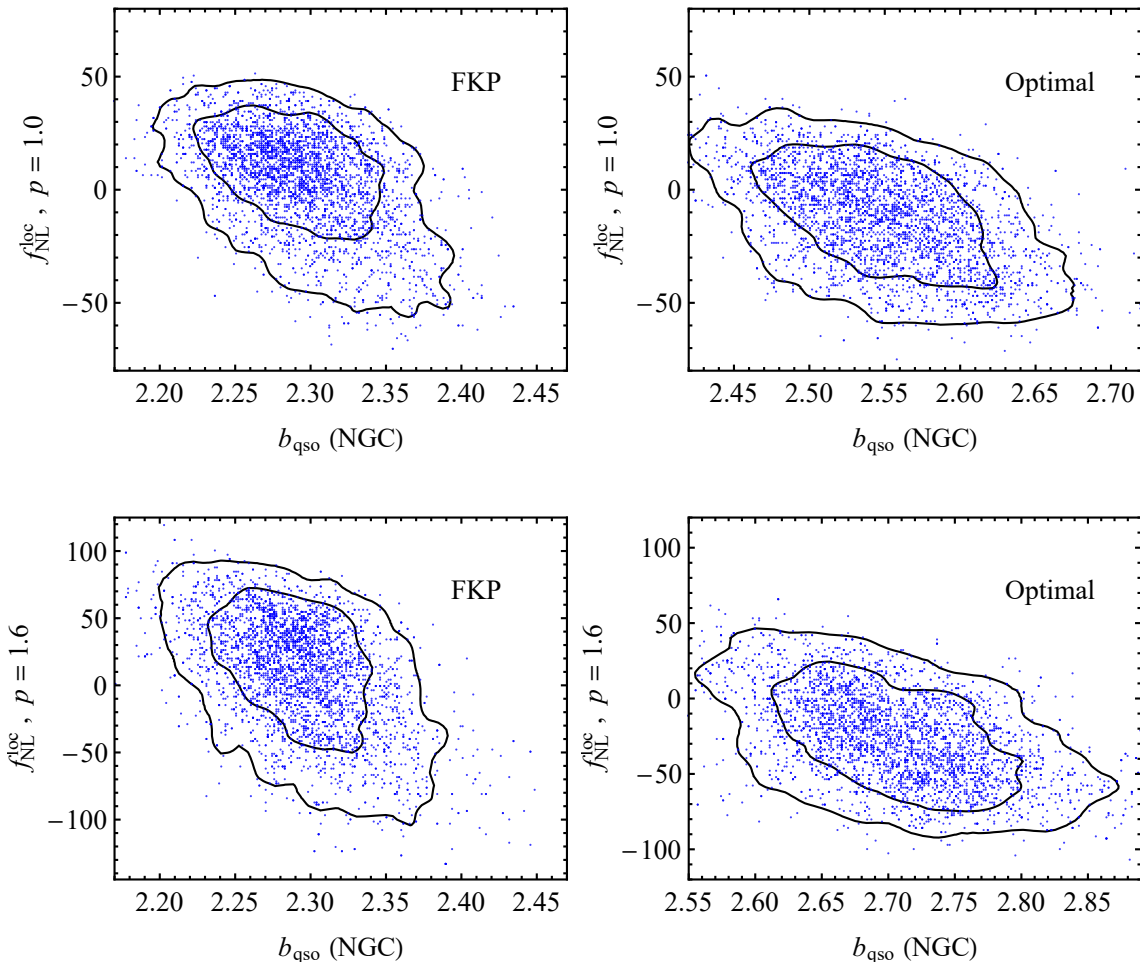
Figure 11: 2-dimensional posterior of $f_{\rm NL}^{\rm loc}$ and QSOs bias in NGC (similar results hold in SGC). The upper panels assume $p = 1.0$, on the right including only FKP weights, on the left with the addition of $f_{\rm NL}^{\rm loc}$ optimal weights. Notice how the 2-dimensional contours shrinks in the optimal case, and the $f_{\rm NL}^{\rm loc}$ and the QSOs bias become less correlated. The lower set of plots show the same results for $p = 1.6$, with exactly the same conclusions.

7 Conclusions

Primordial non Gaussianities of the local form, parametrized by $f_{\rm NL}^{\rm loc}$, leave a unique fingerprint in the clustering of LSS tracers through the presence of scale-dependent bias on large scales. In this work we presented new constraints on $f_{\rm NL}^{\rm loc}$ using the measurements in Fourier space of the clustering of QSOs in DR14 of the eBOSS survey. In order to access the largest available volume we took all the data in the redshift range $0.8 < z < 2.2$ without applying any redshift binning. This allowed us to probe modes up to $k = 3.7 \times 10^{-3}\ h\,{\rm Mpc}^{-1}$. In such a wide redshift range the evolution of the Gaussian part of the signal is quite significant, and differs from the one of the non-Gaussian piece.

We derive a set of weights that maximizes the information content on PNG in the form of a cross correlation between two differently weighted fields, a statistically optimal way to exploit the different evolution of the two signals. Our approach extends the standard FKP weighting, in which all the galaxies are treated the same way from the point of view of their signal content. The optimal weights for PNG up-weight higher redshift objects for two main reasons. First they are more highly biased,

			$f_{\rm NL}^{\rm loc}$ Constraint
NGC	$p = 1.0$	FKP	$-34 \leq f_{\rm NL}^{\rm loc} \leq 61$
		Optimal	$-56 \leq f_{\rm NL}^{\rm loc} \leq 38$
	$p = 1.6$	FKP	$-67 \leq f_{\rm NL}^{\rm loc} \leq 112$
		Optimal	$-87 \leq f_{\rm NL}^{\rm loc} \leq 42$
SGC	$p = 1.0$	FKP	$-64 \leq f_{\rm NL}^{\rm loc} \leq 31$
		Optimal	$-61 \leq f_{\rm NL}^{\rm loc} \leq 26$
	$p = 1.6$	FKP	$-122 \leq f_{\rm NL}^{\rm loc} \leq 63$
		Optimal	$-92 \leq f_{\rm NL}^{\rm loc} \leq 42$
NGC+SGC	$p = 1.0$	FKP	$-39 \leq f_{\rm NL}^{\rm loc} \leq 41$
		Optimal	$-51 \leq f_{\rm NL}^{\rm loc} \leq 21$
	$p = 1.6$	FKP	$-74 \leq f_{\rm NL}^{\rm loc} \leq 81$
		Optimal	$-81 \leq f_{\rm NL}^{\rm loc} \leq 26$

Table 1: Summary of the $f_{\rm NL}^{\rm loc}$ constraints of this work for NGC and SGC separately, as well as their joint analysis.

thus have a higher $f_{\rm NL}^{\rm loc}$ response, and second is that the relative size of the dominant Gaussian term to the non-Gaussian piece is smaller at high redshift since the Gaussian term had less time to grow.

In a spectroscopic survey, one in principle has to integrate the expected signal over the redshift distribution of the galaxies for a proper comparison to the data. However, it is quite often a good approximation to introduce an effective redshfit, defined by the $n(z)$ and the desired set of weights $w(z)$. This is the standard assumption in all galaxy survey analyses, and it has been extensively tested for FKP weights. We checked that the effective redshift approximation is quite accurate even for $f_{\rm NL}^{\rm loc}$ optimal weights, and defined two effective redshifts, one for the monopole and one for the quadrupole.

We then quantified, using a Fisher matrix approach, the expected improvement on $\sigma_{f_{\rm NL}^{\rm loc}}$ of the optimal treatment compared to a standard one, finding 15-40% gain depending on the exact value of the $f_{\rm NL}^{\rm loc}$ response. We also forecasted the possible improvement yielded by including QSOs at $z > 2.2$. Our calculation indicates that $\sigma_{f_{\rm NL}^{\rm loc}} \simeq$ 5-8 could be obtained by final eBOSS QSOs in the redshift range $0.8 < z < 3.5$, if the low k systematics can be kept under control. We find no significant contamination at low k for the $z < 2.2$ QSO sample used in this work.

The exact value of the QSOs response is not known, and can be parametrized by a single number p (higher p means smaller $f_{\rm NL}^{\rm loc}$ signal), which the optimal weights depend on. In this work we considered $p = 1.0$ and 1.6, with the former value valid if QSOs halo occupation is random, and the latter if QSOs

occupy recent merger halos [18]. Our current constraints can be summarized as $-51 \leq f_{\mathrm{NL}}^{\mathrm{loc}} \leq 21$ at 95% confidence level for $p = 1.0$, and they degrade to $-81 \leq f_{\mathrm{NL}}^{\mathrm{loc}} \leq 26$ for $p = 1.6$. It is also worth stressing that the optimal analysis makes the difference between the $p = 1.0$ and $p = 1.6$ case much smaller than in a standard approach. The constraints on PNG presented here are some of the tightest ever obtained using tracers of LSS.

To conclude, in this work we demonstrated the importance of optimal signal weighting in order to extract the maximum information from the data. This required prior analytic knowledge of the signal one is trying to measure, and it reinforces the need for stronger connection between the theory and data analysis for primordial non Gaussianity. We focused on Primordial Non Gaussianities in the power spectrum, but our approach can be straightforwardly extended to any other cosmological parameter and summary statistics. We will return to these interesting questions in future work.

A   The power spectrum quadropole

In the main text we included only the monopole of the power spectrum in the data analysis. This was motivated by the anomalous excess power we observe in the quadrupole of the data. In Figure 12 we show the power spectrum quadrupole in NGC, point with errorbars (dotted for negative values), compared to the theoretical prediction for $f_{\mathrm{NL}}^{\mathrm{loc}} = 0$ and $f_{\mathrm{NL}}^{\mathrm{loc}} = -51, 21$, which correspond to the $\pm 95\%$ values of $f_{\mathrm{NL}}^{\mathrm{loc}}$ in the analysis on the monopole data. Clearly even for such high value of PNG the quadrupole data are inconsistent with the theoretical model, and should therefore be neglected due to their covariance with the monopole measurements.

References

[1] J. Maldacena, *Non-gaussian features of primordial fluctuations in single field inflationary models*, *Journal of High Energy Physics* **5** (2003) 013 [`astro-ph/0210603`].
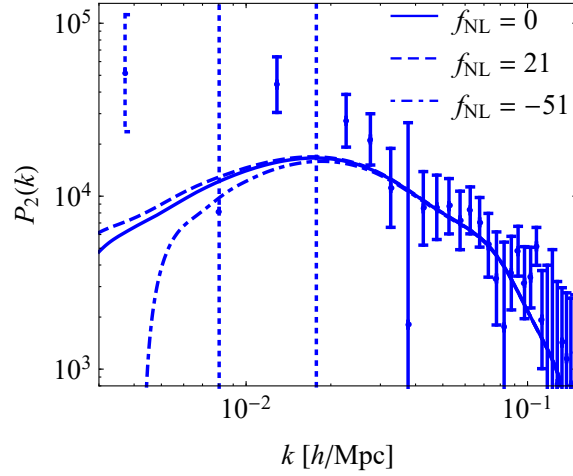
Figure 12: The measurement of the power specturm quadrupole in NGC, point with errorbars (dotted for negative values), in comparison with the model prediction for $f_{\rm NL}^{\rm loc} = 0, -51, 21$.

[2] P. Creminelli and M. Zaldarriaga, *A single-field consistency relation for the three-point function*, J. Cosmology Astropart. Phys. **10** (2004) 006 [`astro-ph/0407059`].

[3] Planck Collaboration, P. A. R. Ade, N. Aghanim, M. Arnaud, F. Arroja, M. Ashdown et al., *Planck 2015 results. XVII. Constraints on primordial non-Gaussianity*, A&A **594** (2016) A17 [`1502.01592`].

[4] D. Baumann, M. G. Jackson, P. Adshead, A. Amblard, A. Ashoorioon, N. Bartolo et al., *Probing Inflation with CMB Polarization*, in *American Institute of Physics Conference Series* (S. Dodelson, D. Baumann, A. Cooray, J. Dunkley, A. Fraisse, M. G. Jackson et al., eds.), vol. 1141 of *American Institute of Physics Conference Series*, pp. 10–120, June, 2009, `0811.3919`, DOI.

[5] K. N. Abazajian, P. Adshead, Z. Ahmed, S. W. Allen, D. Alonso, K. S. Arnold et al., *CMB-S4 Science Book, First Edition*, ArXiv e-prints (2016) [`1610.02743`].

[6] O. Doré, J. Bock, M. Ashby, P. Capak, A. Cooray, R. de Putter et al., *Cosmology with the SPHEREX All-Sky Spectral Survey*, ArXiv e-prints (2014) [`1412.4872`].

[7] D. Yamauchi, K. Takahashi and M. Oguri, *Constraining primordial non-Gaussianity via a multitracer technique with surveys by Euclid and the Square Kilometre Array*, Phys. Rev. D **90** (2014) 083520 [`1407.5453`].

[8] L. D. Ferramacho, M. G. Santos, M. J. Jarvis and S. Camera, *Radio galaxy populations and the multitracer technique: pushing the limits on primordial non-Gaussianity*, MNRAS **442** (2014) 2511 [`1402.2290`].

[9] S. Ferraro and K. M. Smith, *Using large scale structure to measure f_{NL} , g_{NL} and τ_{NL}*, Phys. Rev. D **91** (2015) 043506 [`1408.3126`].

[10] A. Raccanelli, O. Doré and N. Dalal, *Optimization of spectroscopic surveys for testing non-Gaussianity*, J. Cosmology Astropart. Phys. **8** (2015) 034 [`1409.1927`].

[11] S. Camera, M. G. Santos and R. Maartens, *Probing primordial non-Gaussianity with SKA galaxy redshift surveys: a fully relativistic analysis*, MNRAS **448** (2015) 1035 [`1409.8286`].

[12] D. Alonso and P. G. Ferreira, *Constraining ultralarge-scale cosmology with multiple tracers in optical and radio surveys*, Phys. Rev. D **92** (2015) 063525 [`1507.03550`].

[13] M. Tucci, V. Desjacques and M. Kunz, *Cosmic infrared background anisotropies as a window into primordial non-Gaussianity*, MNRAS **463** (2016) 2046 [`1606.02323`].

[14] R. de Putter and O. Doré, *Designing an inflation galaxy survey: How to measure σ (f_{NL})∼1 using scale-dependent galaxy bias*, Phys. Rev. D **95** (2017) 123513.

[15] D. Karagiannis, A. Lazanu, M. Liguori, A. Raccanelli, N. Bartolo and L. Verde, *Constraining primordial non-Gaussianity with bispectrum and power spectrum from upcoming optical and radio surveys*, MNRAS **478** (2018) 1341 [`1801.09280`].

[16] N. Dalal, O. Doré, D. Huterer and A. Shirokov, *Imprints of primordial non-Gaussianities on large-scale structure: Scale-dependent bias and abundance of virialized objects*, Phys. Rev. D **77** (2008) 123514 [`0710.4560`].

[17] S. Matarrese and L. Verde, *The Effect of Primordial Non-Gaussianity on Halo Bias*, ApJ **677** (2008) L77 [`0801.4826`].

[18] A. Slosar, C. Hirata, U. Seljak, S. Ho and N. Padmanabhan, *Constraints on local primordial non-Gaussianity from large scale structure*, J. Cosmology Astropart. Phys. **8** (2008) 031 [`0805.3580`].

[19] V. Desjacques and U. Seljak, *Primordial non-Gaussianity from the large-scale structure*, Classical and Quantum Gravity **27** (2010) 124011 [`1003.5020`].

[20] M. Alvarez, T. Baldauf, J. R. Bond, N. Dalal, R. de Putter, O. Doré et al., *Testing Inflation with Large Scale Structure: Connecting Hopes with Reality*, ArXiv e-prints (2014) [`1412.4671`].

[21] U. Seljak, *Extracting Primordial Non-Gaussianity without Cosmic Variance*, Physical Review Letters **102** (2009) 021302 [`0807.1770`].

[22] P. McDonald and U. Seljak, *How to evade the sample variance limit on measurements of redshift-space distortions*, J. Cosmology Astropart. Phys. **10** (2009) 007 [`0810.0323`].

[23] N. Hamaus, U. Seljak and V. Desjacques, *Optimal constraints on local primordial non-Gaussianity from the two-point statistics of large-scale structure*, Phys. Rev. D **84** (2011) 083509 [`1104.2321`].

[24] E. Castorina, Y. Feng, U. Seljak and F. Villaescusa-Navarro, *Primordial non-Gaussianities and zero bias tracers of the Large Scale Structure*, ArXiv e-prints (2018) [`1803.11539`].

[25] A. J. Ross, W. J. Percival, A. Carnero, G.-b. Zhao, M. Manera, A. Raccanelli et al., *The clustering of galaxies in the SDSS-III DR9 Baryon Oscillation Spectroscopic Survey: constraints on primordial non-Gaussianity*, MNRAS **428** (2013) 1116 [`1208.1491`].

[26] T. Giannantonio, A. J. Ross, W. J. Percival, R. Crittenden, D. Bacher, M. Kilbinger et al., *Improved primordial non-Gaussianity constraints from measurements of galaxy clustering and the integrated Sachs-Wolfe effect*, Phys. Rev. D **89** (2014) 023511 [`1303.1349`].

[27] B. Leistedt, H. V. Peiris and N. Roth, *Constraints on Primordial Non-Gaussianity from 800 000 Photometric Quasars*, Physical Review Letters **113** (2014) 221301 [`1405.4315`].

[28] S. Ho, N. Agarwal, A. D. Myers, R. Lyons, A. Disbrow, H.-J. Seo et al., *Sloan Digital Sky Survey III photometric quasar clustering: probing the initial conditions of the Universe*, J. Cosmology Astropart. Phys. **5** (2015) 040 [`1311.2597`].

[29] C. L. Bennett, D. Larson, J. L. Weiland, N. Jarosik, G. Hinshaw, N. Odegard et al., *Nine-year Wilkinson Microwave Anisotropy Probe (WMAP) Observations: Final Maps and Results*, ApJS **208** (2013) 20 [`1212.5225`].

[30] D. Karagiannis, T. Shanks and N. P. Ross, *Search for primordial non-Gaussianity in the quasars of SDSS-III BOSS DR9*, MNRAS **441** (2014) 486 [`1310.6716`].

[31] A. J. Ross, W. J. Percival, A. G. Sánchez, L. Samushia, S. Ho, E. Kazin et al., *The clustering of galaxies in the SDSS-III Baryon Oscillation Spectroscopic Survey: analysis of potential systematics*, MNRAS **424** (2012) 564 [`1203.6499`].

[32] A. R. Pullen and C. M. Hirata, *Systematic Effects in Large-Scale Angular Power Spectra of Photometric Quasars and Implications for Constraining Primordial Non-Gaussianity*, PASP **125** (2013) 705 [`1212.4500`].

[33] B. Leistedt, H. V. Peiris, D. J. Mortlock, A. Benoit-Lévy and A. Pontzen, *Estimating the large-scale angular power spectrum in the presence of systematics: a case study of Sloan Digital Sky Survey quasars*, MNRAS **435** (2013) 1857 [`1306.0005`].

[34] B. Leistedt and H. V. Peiris, *Exploiting the full potential of photometric quasar surveys: optimal power spectra through blind mitigation of systematics*, MNRAS **444** (2014) 2 [`1404.6530`].

[35] B. Kalus, W. J. Percival, D. J. Bacon, E. M. Mueller, L. Samushia, L. Verde et al., *A map-based method for eliminating systematic modes from galaxy clustering power spectra with application to BOSS*, MNRAS **482** (2019) 453 [1806.02789].

[36] T. Giannantonio and W. J. Percival, *Using correlations between cosmic microwave background lensing and large-scale structure to measure primordial non-Gaussianity*, MNRAS **441** (2014) L16 [1312.5154].

[37] M. Schmittfull and U. Seljak, *Parameter constraints from cross-correlation of CMB lensing with galaxy clustering*, ArXiv e-prints (2017) [1710.09465].

[38] F. Zhu, N. Padmanabhan and M. White, *Optimal redshift weighting for baryon acoustic oscillations*, MNRAS **451** (2015) 236 [1411.1424].

[39] F. Zhu, N. Padmanabhan, M. White, A. J. Ross and G. Zhao, *Redshift weights for baryon acoustic oscillations: application to mock galaxy catalogues*, MNRAS **461** (2016) 2867 [1604.01050].

[40] R. Ruggeri, W. J. Percival, H. Gil-Marín, F. Zhu, G.-B. Zhao and Y. Wang, *Optimal redshift weighting for redshift-space distortions*, MNRAS **464** (2017) 2698 [1602.05195].

[41] K. S. Dawson, J.-P. Kneib, W. J. Percival, S. Alam, F. D. Albareti, S. F. Anderson et al., *The SDSS-IV Extended Baryon Oscillation Spectroscopic Survey: Overview and Early Data*, AJ **151** (2016) 44 [1508.04473].

[42] R. Ruggeri, W. J. Percival, H. Gil Marin, F. Beutler, E. M. Mueller, F. Zhu et al., *The clustering of the SDSS-IV extended Baryon Oscillation Spectroscopic Survey DR14 quasar sample: measuring the evolution of the growth rate using redshift space distortions between redshift 0.8 and 2.2*, ArXiv e-prints (2018) [1801.02891].

[43] F. Zhu, N. Padmanabhan, A. J. Ross, M. White, W. J. Percival, R. Ruggeri et al., *The clustering of the SDSS-IV extended Baryon Oscillation Spectroscopic Survey DR14 quasar sample: Measuring the anisotropic Baryon Acoustic Oscillations with redshift weights*, ArXiv e-prints (2018) [1801.03038].

[44] G.-B. Zhao, Y. Wang, S. Saito, D. Wang, A. J. Ross, F. Beutler et al., *The clustering of galaxies in the completed sdss-iii baryon oscillation spectroscopic survey: tomographic bao analysis of dr12 combined sample in fourier space*, MNRAS **466** (2017) 762 [1607.03153].

[45] P. Zarrouk, E. Burtin, H. Gil-Marín, A. J. Ross, R. Tojeiro, I. Pâris et al., *The clustering of the SDSS-IV extended Baryon Oscillation Spectroscopic Survey DR14 quasar sample: measurement of the growth rate of structure from the anisotropic correlation function between redshift 0.8 and 2.2*, MNRAS **477** (2018) 1639 [1801.03062].

[46] D. Wang, G.-B. Zhao, Y. Wang, W. J. Percival, R. Ruggeri, F. Zhu et al., *The clustering of the SDSS-IV extended Baryon Oscillation Spectroscopic Survey DR14 quasar sample: anisotropic Baryon Acoustic Oscillations measurements in Fourier-space with optimal redshift weights*, MNRAS **477** (2018) 1528 [1801.03077].

[47] E.-M. Mueller, W. J. Percival and R. Ruggeri, *Optimising primordial non-Gaussianity measurements from galaxy surveys*, ArXiv e-prints (2017) [1702.05088].

[48] H. A. Feldman, N. Kaiser and J. A. Peacock, *Power-spectrum analysis of three-dimensional redshift surveys*, ApJ **426** (1994) 23 [astro-ph/9304022].

[49] B. Abolfathi, D. S. Aguado, G. Aguilar, C. Allende Prieto, A. Almeida, T. Tasnim Ananna et al., *The Fourteenth Data Release of the Sloan Digital Sky Survey: First Spectroscopic Data from the Extended Baryon Oscillation Spectroscopic Survey and from the Second Phase of the Apache Point Observatory Galactic Evolution Experiment*, ApJS **235** (2018) 42 [1707.09322].

[50] M. Biagetti, T. Lazeyras, T. Baldauf, V. Desjacques and F. Schmidt, *Verifying the consistency relation for the scale-dependent bias from local primordial non-Gaussianity*, MNRAS **468** (2017) 3277 [1611.04901].

[51] B. A. Reid, L. Verde, K. Dolag, S. Matarrese and L. Moscardini, *Non-Gaussian halo assembly bias*, J. Cosmology Astropart. Phys. **7** (2010) 013 [1004.1637].

[52] N. Kaiser, *Clustering in real space and in redshift space*, MNRAS **227** (1987) 1.

[53] M. Tegmark, *How to measure CMB power spectra without losing information*, Phys. Rev. D **55** (1997) 5895 [`astro-ph/9611174`].

[54] J. R. Bond, A. H. Jaffe and L. Knox, *Radical Compression of Cosmic Microwave Background Data*, ApJ **533** (2000) 19 [`astro-ph/9808264`].

[55] M. Tegmark, *Measuring Cosmological Parameters with Galaxy Surveys*, Physical Review Letters **79** (1997) 3806 [`astro-ph/9706198`].

[56] M. Tegmark, A. N. Taylor and A. F. Heavens, *Karhunen-Loève Eigenvalue Problems in Cosmology: How Should We Tackle Large Data Sets?*, ApJ **480** (1997) 22 [`astro-ph/9603021`].

[57] M. Tegmark, A. J. S. Hamilton, M. A. Strauss, M. S. Vogeley and A. S. Szalay, *Measuring the Galaxy Power Spectrum with Future Redshift Surveys*, ApJ **499** (1998) 555 [`astro-ph/9708020`].

[58] L. R. Abramo, L. F. Secco and A. Loureiro, *Fourier analysis of multitracer cosmological surveys*, MNRAS **455** (2016) 3871 [`1505.04106`].

[59] K. Yamamoto, M. Nakamichi, A. Kamino, B. A. Bassett and H. Nishioka, *A measurement of the quadrupole power spectrum in the clustering of the 2df qso survey*, PASJ **58** (2006) 93 [`astro-ph/0505115`].

[60] D. Bianchi, H. Gil-Marín, R. Ruggeri and W. J. Percival, *Measuring line-of-sight-dependent fourier-space clustering using ffts*, MNRAS **453** (2015) L11 [`1505.05341`].

[61] R. Scoccimarro, *Fast estimators for redshift-space clustering*, Phys. Rev. D **92** (2015) 083532 [`1506.02729`].

[62] N. Hand, Y. Li, Z. Slepian and U. Seljak, *An optimal fft-based anisotropic power spectrum estimator*, J. Cosmology Astropart. Phys. **7** (2017) 002 [`1704.02357`].

[63] F. Beutler, E. Castorina and P. Zhang, *Interpreting measurements of the anisotropic galaxy power spectrum*, ArXiv e-prints (2018) [`1810.05051`].

[64] M. R. Blanton, M. A. Bershady, B. Abolfathi, F. D. Albareti, C. Allende Prieto, A. Almeida et al., *Sloan Digital Sky Survey IV: Mapping the Milky Way, Nearby Galaxies, and the Distant Universe*, AJ **154** (2017) 28 [`1703.00052`].

[65] S. A. Smee, J. E. Gunn, A. Uomoto, N. Roe, D. Schlegel, C. M. Rockosi et al., *The Multi-object, Fiber-fed Spectrographs for the Sloan Digital Sky Survey and the Baryon Oscillation Spectroscopic Survey*, AJ **146** (2013) 32 [`1208.2233`].

[66] J. E. Gunn, W. A. Siegmund, E. J. Mannery, R. E. Owen, C. L. Hull, R. F. Leger et al., *The 2.5 m Telescope of the Sloan Digital Sky Survey*, AJ **131** (2006) 2332 [`astro-ph/0602326`].

[67] M. Ata, F. Baumgarten, J. Bautista, F. Beutler, D. Bizyaev, M. R. Blanton et al., *The clustering of the SDSS-IV extended Baryon Oscillation Spectroscopic Survey DR14 quasar sample: First measurement of Baryon Acoustic Oscillations between redshift 0.8 and 2.2*, ArXiv e-prints (2017) [`1705.06373`].

[68] P. Laurent, S. Eftekharzadeh, J.-M. Le Goff, A. Myers, E. Burtin, M. White et al., *Clustering of quasars in SDSS-IV eBOSS: study of potential systematics and bias determination*, J. Cosmology Astropart. Phys. **7** (2017) 017 [`1705.04718`].

[69] S. A. Rodríguez-Torres, J. Comparat, F. Prada, G. Yepes, E. Burtin, P. Zarrouk et al., *Clustering of quasars in the first year of the SDSS-IV eBOSS survey: interpretation and halo occupation distribution*, MNRAS **468** (2017) 728 [`1612.06918`].

[70] J. Hou, A. G. Sánchez, R. Scoccimarro, S. Salazar-Albornoz, E. Burtin, H. Gil-Marín et al., *The clustering of the SDSS-IV extended Baryon Oscillation Spectroscopic Survey DR14 quasar sample: anisotropic clustering analysis in configuration-space*, ArXiv e-prints (2018) [`1801.02656`].

[71] H. Gil-Marín, J. Guy, P. Zarrouk, E. Burtin, C.-H. Chuang, W. J. Percival et al., *The clustering of the SDSS-IV extended Baryon Oscillation Spectroscopic Survey DR14 quasar sample: structure growth rate measurement from the anisotropic quasar power spectrum in the redshift range $0.8 < z < 2.2$*, MNRAS **477** (2018) 1604 [`1801.02689`].

[72] I. Pâris, P. Petitjean, N. P. Ross, A. D. Myers, É. Aubourg, A. Streblyanska et al., *The Sloan Digital Sky Survey Quasar Catalog: Twelfth data release*, A&A **597** (2017) A79 [`1608.06483`].

[73] D. G. York, J. Adelman, J. E. Anderson, Jr., S. F. Anderson, J. Annis, N. A. Bahcall et al., *The Sloan Digital Sky Survey: Technical Summary*, AJ **120** (2000) 1579 [`astro-ph/0006396`].

[74] K. N. Abazajian, J. K. Adelman-McCarthy, M. A. Agüeros, S. S. Allam, C. Allende Prieto, D. An et al., *The Seventh Data Release of the Sloan Digital Sky Survey*, ApJS **182** (2009) 543 [`0812.0649`].

[75] D. J. Eisenstein, D. H. Weinberg, E. Agol, H. Aihara, C. Allende Prieto, S. F. Anderson et al., *SDSS-III: Massive Spectroscopic Surveys of the Distant Universe, the Milky Way, and Extra-Solar Planetary Systems*, AJ **142** (2011) 72 [`1101.1529`].

[76] K. S. Dawson, D. J. Schlegel, C. P. Ahn, S. F. Anderson, É. Aubourg, S. Bailey et al., *The Baryon Oscillation Spectroscopic Survey of SDSS-III*, AJ **145** (2013) 10 [`1208.0022`].

[77] H. Aihara, C. Allende Prieto, D. An, S. F. Anderson, É. Aubourg, E. Balbinot et al., *The Eighth Data Release of the Sloan Digital Sky Survey: First Data from SDSS-III*, ApJS **193** (2011) 29 [`1101.1559`].

[78] E. L. Wright, P. R. M. Eisenhardt, A. K. Mainzer, M. E. Ressler, R. M. Cutri, T. Jarrett et al., *The Wide-field Infrared Survey Explorer (WISE): Mission Description and Initial On-orbit Performance*, AJ **140** (2010) 1868 [`1008.0031`].

[79] A. D. Myers, N. Palanque-Delabrouille, A. Prakash, I. Pâris, C. Yeche, K. S. Dawson et al., *The SDSS-IV Extended Baryon Oscillation Spectroscopic Survey: Quasar Target Selection*, ApJS **221** (2015) 27 [`1508.04472`].

[80] A. D. Myers, R. J. Brunner, R. C. Nichol, G. T. Richards, D. P. Schneider and N. A. Bahcall, *Clustering Analyses of 300,000 Photometrically Classified Quasars. I. Luminosity and Redshift Evolution in Quasar Bias*, ApJ **658** (2007) 85 [`astro-ph/0612190`].

[81] N. P. Ross, A. D. Myers, E. S. Sheldon, C. Yèche, M. A. Strauss, J. Bovy et al., *The SDSS-III Baryon Oscillation Spectroscopic Survey: Quasar Target Selection for Data Release Nine*, ApJS **199** (2012) 3 [`1105.0606`].

[82] Y. Shen, W. N. Brandt, G. T. Richards, K. D. Denney, J. E. Greene, C. J. Grier et al., *The Sloan Digital Sky Survey Reverberation Mapping Project: Velocity Shifts of Quasar Emission Lines*, ApJ **831** (2016) 7 [`1602.03894`].

[83] L. Anderson, É. Aubourg, S. Bailey, F. Beutler, V. Bhardwaj, M. Blanton et al., *The clustering of galaxies in the SDSS-III Baryon Oscillation Spectroscopic Survey: baryon acoustic oscillations in the Data Releases 10 and 11 Galaxy samples*, MNRAS **441** (2014) 24 [`1312.4877`].

[84] B. A. Reid, H.-J. Seo, A. Leauthaud, J. L. Tinker and M. White, *A 2.5 per cent measurement of the growth rate from small-scale redshift space clustering of SDSS-III CMASS galaxies*, MNRAS **444** (2014) 476 [`1404.3742`].

[85] C. Hahn, R. Scoccimarro, M. R. Blanton, J. L. Tinker and S. A. Rodríguez-Torres, *The Effect of Fiber Collisions on the Galaxy Power Spectrum Multipoles*, MNRAS **467** (2017) 1940 [`1609.01714`].

[86] B. Reid, S. Ho, N. Padmanabhan, W. J. Percival, J. Tinker, R. Tojeiro et al., *SDSS-III Baryon Oscillation Spectroscopic Survey Data Release 12: galaxy target selection and large-scale structure catalogues*, MNRAS **455** (2016) 1553 [`1509.06529`].

[87] C.-H. Chuang, F.-S. Kitaura, F. Prada, C. Zhao and G. Yepes, *EZmocks: extending the Zel'dovich approximation to generate mock galaxy catalogues with accurate clustering statistics*, MNRAS **446** (2015) 2621 [`1409.1124`].

[88] F.-S. Kitaura, S. Rodríguez-Torres, C.-H. Chuang, C. Zhao, F. Prada, H. Gil-Marín et al., *The clustering of galaxies in the SDSS-III Baryon Oscillation Spectroscopic Survey: mock galaxy catalogues for the BOSS Final Data Release*, MNRAS **456** (2016) 4156 [`1509.06400`].

[89] S. Alam, M. Ata, S. Bailey, F. Beutler, D. Bizyaev, J. A. Blazek et al., *The clustering of galaxies in the completed SDSS-III Baryon Oscillation Spectroscopic Survey: cosmological analysis of the DR12 galaxy sample*, MNRAS **470** (2017) 2617 [`1607.03155`].

[90] J. Carlson and M. White, *Embedding Realistic Surveys in Simulations Through Volume Remapping*, ApJS **190** (2010) 311 [`1003.3178`].

[91] Planck Collaboration, N. Aghanim, Y. Akrami, M. Ashdown, J. Aumont, C. Baccigalupi et al., *Planck 2018 results. VI. Cosmological parameters*, ArXiv e-prints (2018) [`1807.06209`].

[92] F. Beutler, S. Saito, H.-J. Seo, J. Brinkmann, K. S. Dawson, D. J. Eisenstein et al., *The clustering of galaxies in the SDSS-III Baryon Oscillation Spectroscopic Survey: testing gravity with redshift space distortions using the power spectrum multipoles*, MNRAS **443** (2014) 1065 [`1312.4611`].

[93] F. Beutler, H.-J. Seo, S. Saito, C.-H. Chuang, A. J. Cuesta, D. J. Eisenstein et al., *The clustering of galaxies in the completed sdss-iii baryon oscillation spectroscopic survey: anisotropic galaxy clustering in fourier space*, MNRAS **466** (2017) 2242 [`1607.03150`].

[94] J. N. Grieb, A. G. Sánchez, S. Salazar-Albornoz, R. Scoccimarro, M. Crocce, C. Dalla Vecchia et al., *The clustering of galaxies in the completed SDSS-III Baryon Oscillation Spectroscopic Survey: Cosmological implications of the Fourier space wedges of the final sample*, MNRAS **467** (2017) 2085 [`1607.03143`].

[95] R. W. Hockney and J. W. Eastwood, *Computer Simulation Using Particles*. 1981.

[96] E. Sefusatti, M. Crocce, R. Scoccimarro and H. M. P. Couchman, *Accurate estimators of correlation functions in fourier space*, MNRAS **460** (2016) 3624 [`1512.07295`].

[97] Y. P. Jing, *Correcting for the alias effect when measuring the power spectrum using a fast fourier transform*, ApJ **620** (2005) 559 [`astro-ph/0409240`].

[98] N. Hand, Y. Feng, F. Beutler, Y. Li, C. Modi, Z. Slepian et al., *nbodykit: a massively parallel large-scale structure toolkit*, ApJ (2017) .

[99] J. C. Jackson, *A critique of rees's theory of primordial gravitational radiation*, MNRAS **156** (1972) 1P [`0810.3908`].

[100] N. Hand and Y. Feng, *classylss*, Nov., 2017. 10.5281/zenodo.1051256.

[101] D. Blas, J. Lesgourgues and T. Tram, *The Cosmic Linear Anisotropy Solving System (CLASS). Part II: Approximation schemes*, J. Cosmology Astropart. Phys. **7** (2011) 034 [`1104.2933`].

[102] H. Gil-Marín, W. J. Percival, J. R. Brownstein, C.-H. Chuang, J. N. Grieb, S. Ho et al., *The clustering of galaxies in the sdss-iii baryon oscillation spectroscopic survey: Rsd measurement from the los-dependent power spectrum of dr12 boss galaxies*, MNRAS **460** (2016) 4188 [`1509.06386`].

[103] M. J. Wilson, J. A. Peacock, A. N. Taylor and S. de la Torre, *Rapid modelling of the redshift-space power spectrum multipoles for a masked density field*, MNRAS **464** (2017) 3121 [`1511.07799`].

[104] E. Castorina and M. White, *Beyond the plane-parallel approximation for redshift surveys*, MNRAS **476** (2018) 4403 [`1709.09730`].

[105] E. Castorina and M. White, *The Zeldovich approximation and wide-angle redshift-space distortions*, MNRAS (2018) [`1803.08185`].

[106] Z. Vlah, E. Castorina and M. White, *The Gaussian streaming model and convolution Lagrangian effective field theory*, J. Cosmology Astropart. Phys. **12** (2016) 007 [`1609.02908`].

[107] G.-B. Zhao, Y. Wang, S. Saito, H. Gil-Marín, W. J. Percival, D. Wang et al., *The clustering of the SDSS-IV extended Baryon Oscillation Spectroscopic Survey DR14 quasar sample: a tomographic measurement of cosmic structure growth and expansion rate based on optimal redshift weights*, ArXiv e-prints (2018) [`1801.03043`].

[108] C. Alcock and B. Paczynski, *An evolution free test for non-zero cosmological constant*, Nature **281** (1979) 358.

[109] Planck Collaboration, Y. Akrami, F. Arroja, M. Ashdown, J. Aumont, C. Baccigalupi et al., *Planck 2018 results. I. Overview and the cosmological legacy of Planck*, ArXiv e-prints (2018) [`1807.06205`].

[110] J. Hartlap, P. Simon and P. Schneider, *Why your model parameter confidences might be too optimistic. Unbiased estimation of the inverse covariance matrix*, A&A **464** (2007) 399 [`astro-ph/0608064`].

[111] W. J. Percival, A. J. Ross, A. G. Sánchez, L. Samushia, A. Burden, R. Crittenden et al., *The clustering of Galaxies in the SDSS-III Baryon Oscillation Spectroscopic Survey: including covariance matrix errors*, MNRAS **439** (2014) 2531 [`1312.4841`].

[112] R. H. Byrd, P. Lu, J. Nocedal and C. Zhu, *A limited memory algorithm for bound constrained optimization*, SIAM J. Sci. Comput. **16** (1995) 1190.

[113] D. Foreman-Mackey, D. W. Hogg, D. Lang and J. Goodman, *emcee: The MCMC Hammer*, PASP **125** (2013) 306 [`1202.3665`].

[114] M. Tegmark and P. J. E. Peebles, *The Time Evolution of Bias*, ApJ **500** (1998) L79 [`astro-ph/9804067`].